CrossMark

J. Fluid Mech. (2017), *vol.* 827, *pp.* 572–613. © Cambridge University Press 2017
doi:10.1017/jfm.2017.495

On the dynamics of vortex–droplet interactions, dispersion and breakup in a coaxial swirling flow

Kuppuraj Rajamanickam[1] **and Saptarshi Basu**[1,†]

[1]Department of Mechanical Engineering, Indian Institute of Science, Bangalore-560012, India

(Received 22 February 2017; revised 22 May 2017; accepted 16 July 2017;
first published online 30 August 2017)

This paper discusses the fundamental mechanisms of vortex–droplet interactions leading to flow distortion, droplet dispersion and breakup in a complex swirling gas flow field. In particular, the way in which the location of droplet injection determines the degree of inhomogeneous dispersion and breakup modes has been elucidated in detail using high-fidelity laser diagnostics. The droplets are injected as monodispersed streams at various spatial locations such as the vortex breakdown bubble and the shear layers (inner and outer) exhibited by the swirling flow. Simultaneous time-resolved particle image velocimetry (3500 frames s^{-1}) and high-speed shadowgraphy measurements are employed to delineate the two-phase interaction dynamics. These measurements have been used to evaluate the fluctuations in instantaneous circulation strength Γ' caused by the flow field eddies and the resultant angular dispersion in the droplet trajectories θ'. The droplet–flow interactions show two-way coupling at low momentum ratios (*MR*) and strong one-way coupling at high momentum ratios. The gas phase flow field is globally altered at low airflow rates (low *MR*) due to impact of droplets with the vortex core. The flow perturbation is found to be minimal and mainly local at high airflow rates (high *MR*). Spectral coherence analysis is carried out to understand the correlation between eddy circulation strength Γ' and droplet dispersion θ'. The droplet dispersion shows strong coherence with the flow in certain frequency bands. Subsequently, proper orthogonal decomposition (POD) is implemented to elucidate the governing instability mechanism and frequency signatures associated with the turbulent coherent structures. The POD results suggest dominance of the Kelvin–Helmholtz (KH) instability mode (axial and azimuthal shear). The frequency range pertaining to high coherence between dispersion and circulation shows good agreement with KH instability quantified from POD analysis. The droplets injected at the inner shear layer (ISL) and outer shear layer (OSL) show different interaction dynamics. For instance, droplet dispersion at the OSL exhibits secondary frequency (shedding mode) coupling in addition to the KH mode, whereas ISL injection couples only in a single narrow frequency band (i.e. KH mode). Further, high-speed shadow imaging (7500 frames s^{-1}) is employed to visualize the breakup dynamics of the droplets. The effect of coherent structures on the droplet breakup modes is shown as a function of the Weber number (*We*) defined based on the circulation strength. The wide fluctuations caused in the instantaneous circulation strength lead to different breakup modes (bag, multimodal, shear thinning, catastrophic) even for fixed airflow rates. These fluctuations also lead to inhomogeneous spatial dispersion of the droplets in the swirling gas flow field. We are able to present the dispersion contours in terms of the Stokes number and a

† Email address for correspondence: sbasu@mecheng.iisc.ernet.in

https://doi.org/10.1017/jfm.2017.495 Published online by Cambridge University Press

spatial homogeneity parameter. In essence, the dispersion inhomogeneity is found to be a strong function of the injection location, the phase relationship with the eddies and the momentum ratio (*MR*).

Key words: breakup/coalescence, drops and bubbles, vortex interactions

1. Introduction

The interaction dynamics, breakup and dispersion of droplets in a coflowing gas medium are ubiquitous to many industrial applications. In particular, droplet–flow interactions attract special attention in liquid-fuelled gas turbine combustion systems. In gas turbines, fuel droplets are injected in the form of sprays in the high-speed coaxial swirling gas phase (Wang, McDonell & Samuelsen 1993; Moin & Apte 2006; Boileau *et al.* 2008). Here, the momentum associated with the gas phase is usually several orders higher than that of the liquid phase, which results in the imposition of inherent gas phase instabilities on the liquid phase, leading to primarily one-way coupling. The injected droplets hence couple tightly with the highly turbulent swirling flow, leading to significant dispersion (Gu, Basu & Kumar 2012) and multimodal secondary breakups. The resultant spatially inhomogeneous dispersion process is of particular importance in combustion research since it will usually lead to spatiotemporal fluctuations in the mixing. The mixing fluctuations affect the combustion efficiency and emissions (Lefebvre 2010), and may lead to combustion instabilities.

The complexity and the influence of several coupled parameters prohibit a complete understanding of how the droplets interact with the flow (especially the large-scale coherent structures). Studies carried out by Shirolkar, Coimbra & McQuay (1996), Crowe, Sommerfeld & Tsuji (1998) and Balachandar & Eaton (2010) highlighted the dynamic behaviour of dispersion due to the presence of large-scale coherent structures in the gas phase. The key parameters identified in droplet–vortex/flow interactions are turbulent fluctuations in both the carrier phase (gas) and the dispersed phase (droplets) with respect to one another (Chung & Troutt 1988; Lazaro & Lasheras 1992; Kulick, Fessler & Eaton 1994) and subsequent clustering of droplets/particles in the small/large-scale eddies (Sirignano 1999; Sankaran & Menon 2002). In particle-laden flows, Elghobashi & Truesdell (1993) and Loth *et al.* (2006) categorized the carrier and dispersed phase interaction in terms of the droplet response time scale (τ_D) and the carrier phase turbulent time scale (τ_k), concisely represented in non-dimensional form by the Stokes number $St = \tau_D/\tau_k$. In dense droplet regions (e.g. near the nozzle), the momentum coupling is identified as two-way (i.e. the carrier phase is influenced by the dispersed phase), whereas in dilute regions (i.e. the far field of the spray nozzle), momentum transfer into the carrier phase is negligible (i.e. one-way coupling). The other important parameter in the dispersion process is the evaporative nature of the liquid phase (as in combustion applications). In evaporating droplets, Aggarwal & Park (1999) pointed out the importance of the droplet life time (τ_t) in addition to the droplet response time scale (τ_D). It has been shown that in situations like droplets interacting with large-scale coherent structures, if $\tau_t \ll \tau_d$, then the dispersion process is altered significantly.

The fundamental interaction mechanisms and dispersion may differ as a function of the flow configuration (combustor geometry, injector design). For instance, most

https://doi.org/10.1017/jfm.2017.495 Published online by Cambridge University Press

gas turbine combustors utilize swirling flows to accomplish intense mixing and flame stability (Lilley 1977). Unlike round jets, in addition to axial shear, swirling jets exhibit centrifugal instabilities (Ribeiro & Whitelaw 1980), which add additional complexities in quantifying the vortex–droplet interaction. The origin of centrifugal instabilities in swirling flows is governed by vortex bubble breakdown (VBB) caused by intense rotation of the fluid (Santhosh, Miglani & Basu 2014). Further, the spatial dispersion of the droplets is significantly affected by the presence of the radial velocity component in swirling jets, i.e. droplets are forced towards the periphery of the flow field (Sanadi, Rajamanickam & Basu 2017). Numerical simulations carried out by Park, Katta & Aggarwal (1998) revealed enhancement of the spatial dispersion of droplets in swirl flows due to the vortex pairing mechanism. Large eddy simulation (LES) studies of droplet dispersion in swirling flows carried out by Sankaran & Menon (2002) revealed the crucial role of the central toroidal recirculation zone (CTRZ) manifested in VBB. They pointed out the spatial clustering behaviour of extremely small-sized droplets ($St \ll 1$) within the vortical region. The droplet size scales pertaining to $St \gg 1$ exhibit radially outward dispersion arising from the large-scale coherent structures. The degree of complexity in coaxial two-phase flow interactions lies in the carrier phase (instability modes, frequency spectrum, etc.). However, most of these studies related to dispersion and clustering are computational in nature without significant experimental backing.

Another parameter of interest is the associated droplet breakup mechanism during interaction with the coherent structures of the swirling flow field. Droplet breakup experiments (Faeth, Hsiang & Wu 1995; Guildenbecher, López-Rivera & Sojka 2009) carried out in high-speed coaxial flow suggest different breakup mechanisms such as bag, sheet thinning, multimodal and catastrophic, to name a few. Wave formation over the droplet surface is considered to be a key parameter governing the breakup mechanism. The nature of the waves and the corresponding length scales are solely dictated by instabilities associated with the carrier phase. Marmottant & Villermaux (2004) have shown the dominance of Kelvin–Helmholtz (KH) waves in droplets subjected to high shear. Flock *et al.* (2012) identified the bag breakup mechanism when droplets interact with the shedding vortices. However, all of these experiments were carried out primarily in non-swirling flow conditions.

Computational and theoretical studies have been conducted to elucidate the flow dynamics of the carrier phase. For instance, Al Taweel & Landau (1977), Danon, Wolfshtein & Hetsroni (1977) and Elghobashi & Abou-Arab (1983) developed a correlation function based on the droplet–droplet and droplet–gas interactions to delineate the effects of modulation of the carrier phase across multiple length scales. However, most models fail to accurately predict the interactions and demand more experimental insight. Since the problem involves interphase momentum coupling, simultaneous two-phase measurements are needed to elucidate the various time and length scales involved in the process. Gillandt, Fritsching & Bauckhage (2001) have used a phase Doppler anemometry (PDA) system to reveal the turbulence modulation in two-phase flows by simultaneous measurement of the droplet size and velocity of both the gas and liquid phases. However, as it is a point measurement technique, PDA has limitations in probing the influence of large-scale flow structures present in a highly turbulent environment. This mandates the need for planar measurement systems such as particle imaging velocimetry (PIV) or interferometric Mie imaging (IMI), to name a few. Sakakibara, Wicker & Eaton (1996) and Khalitov & Longmire (2003) implemented simultaneous PIV measurements in the two-phase flow to evaluate the gas and liquid phase velocities. The recorded PIV images allowed phase separation

https://doi.org/10.1017/jfm.2017.495 Published online by Cambridge University Press

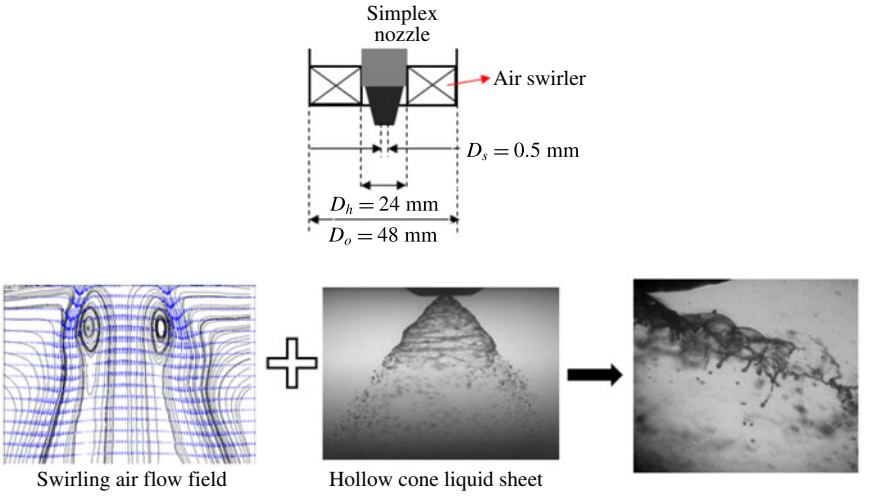

FIGURE 1. (Colour online) Schematic of a standard coaxial atomizer coupled with a swirler.

between the two fluids (i.e. gas and liquid) using a thresholding technique. The phase separated images could be used later to correlate the influence of one fluid over the other, enabling the formulation of relevant universal scales (eddy strength, droplet dispersion angle).

1.1. *Scope of the work*

The literature survey set out in the previous section clearly points towards the lack of understanding of how droplets interact with large-scale coherent structures (vortices) as in a swirling flow field. In particular, an understanding of droplet–vortex interaction in the near field of the swirler is of significant importance. In the near field, the swirling flow exhibits highly complicated structures such as counter-rotating eddies and a precessing vortex core (PVC), to name a few. Since most of the interphase (gas–liquid) momentum exchange occurs in this zone, it is mandatory to precisely probe the physical mechanisms behind droplet dispersion and breakup. The main objective of this work is to identify these physical mechanisms using high-fidelity laser diagnostic techniques.

In this study, we consider a flow geometry similar to lean direct injection (LDI) combustors, where a simplex nozzle and an air swirler are mounted in a coaxial configuration. The simplex nozzle discharges a hollow cone liquid sheet into the swirling air. Due to the shear layer instability, the liquid sheet breaks up into ligaments and droplets (see figure 1). Furthermore, these droplets undergo breakup as a function of local interactions with the flow field (e.g. eddies) (Saha *et al.* 2012). In our previous study (Rajamanickam & Basu 2017), the near-field breakup mechanism and the sizes of the first-generation droplets were elaborated in greater detail.

However, the above-mentioned configuration (figure 1) cannot be used to answer certain questions such as (i) how the injection location of the droplets alters the dispersion/breakup behaviour, (ii) how the gas phase momentum leads to heterogeneous clustering and multimodal breakup of droplets and (iii) how the flow is locally modified on interaction with the droplets. These questions require

https://doi.org/10.1017/jfm.2017.495 Published online by Cambridge University Press

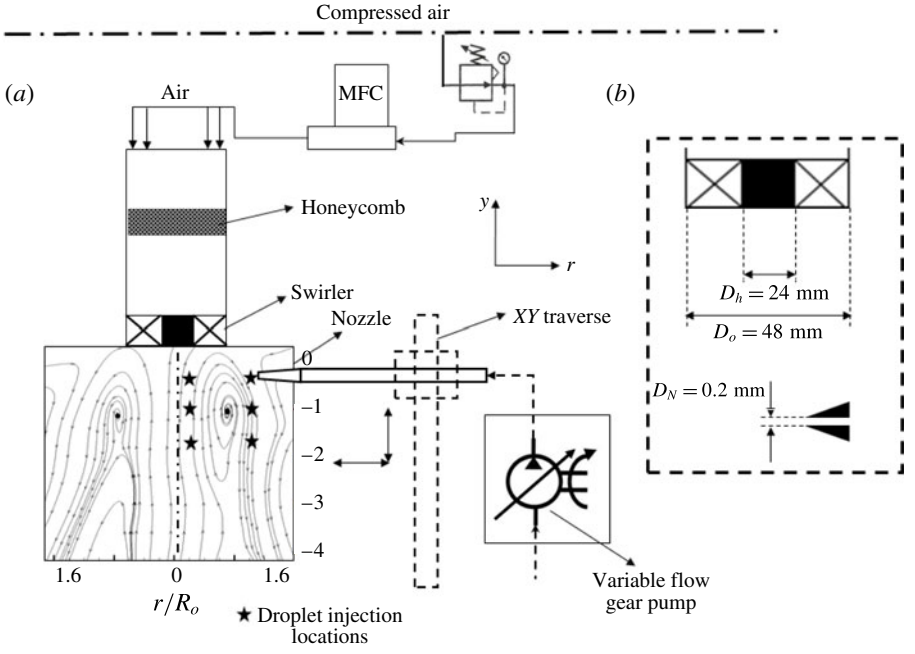

FIGURE 2. (*a*) Schematic of the experimental set-up. A horizontal stream of monodispersed droplets is injected at various axial and radial locations. (*b*) Geometrical details of the swirler and capillary nozzle.

the injection of a monodispersed stream of low-momentum droplets instead of a polydispersed varying cone angle spray. Hence, in the present study, attention is mainly focused on how these well-defined streams of droplets behave in the swirling flow field depending on the injection location.

Although the flow geometry is similar to LDI, in the experiments reported, the simplex nozzle (figure 1) does not discharge any droplets into the flow field. Hence, this study does not attempt to mimic the real-life LDI scenario.

To elucidate the dynamics, as stated earlier, a stream of monodispersed droplets is injected radially at various predefined locations in the flow field (figure 2). The injection point locations are selected based on the maximum shear strength and turbulent kinetic energy (TKE) distributions in the spatial domain (to be shown later). The radial configuration (akin to droplets in cross-flow) allows dilute injection at various locations in the swirling flow field, which is not achievable by coaxial means.

This paper is arranged in the following manner. In § 2, we explain the experimental details, flow conditions and optical diagnostics tools used in this study. Section 3 describes the global flow field characterization (including the time-averaged vorticity contours and the velocity field) using time-resolved PIV. This section provides topological observations on how the flow field becomes altered (i.e. local disruption of the vortex core) with the liquid injection location and the corresponding global droplet response. This also helps to quantify weak and strong interaction flow conditions. Spectral coherence analysis is implemented in § 4 to elucidate how the circulation strengths of the flow and dispersion are coupled in various frequency bands depending on the injection location. Subsequently, the instability modes and their associated

https://doi.org/10.1017/jfm.2017.495 Published online by Cambridge University Press

frequency signatures are extracted using proper orthogonal decomposition (POD) in § 5. Here, the modal coupling between the two phases is delineated with the help of POD analysis applied to the flow field with and without the presence of droplets. The POD enabled us to find that the global droplet dispersion is caused by different distinct flow eigenmodes. In § 6, the local breakup mechanism and the dynamics of the droplets in the presence of gas phase coherent structures are elucidated using a high-speed (7500 frames s^{-1}) shadow imaging technique. This establishes how the vorticity fluctuations can lead to multimodal breakup events even for fixed flow rates. Finally, the spatially inhomogeneous dispersion of the droplets is explained in § 7 along with the possible mechanisms. All of the sections combined together offer a comprehensive understanding of droplet–vortex interactions.

2. Experimental conditions and procedure

The experimental set-up utilized in this study is schematically shown in figure 2. The principal component consists of a vane swirler with a solid central hub. The swirler has six vanes with a vane angle of $\emptyset = 45°$ (other geometric details can be found in figure 2*b*). For all of the experiments, air and water are used as the working fluids. Droplet injection is carried out using a capillary nozzle (radial arrangement) with an orifice diameter of $D_N = 0.25$ mm. The generated droplets are predominantly monodispersed in nature. The droplets are injected as a horizontal stream at specific locations, as indicated in figure 2(*a*). Across all of the experiments, the airflow rate across the swirler is progressively varied from 500 to 3000 lpm, while the liquid flow rate is maintained constant (0.05 lpm). The airflow rate is metered using a thermal mass flow controller (MFC) (make: Alicat Inc., range −0–3000 lpm $\pm$ 0.8 % full scale). The nominal initial size (d_o) of the injected droplets is approximately 500 μm.

2.1. *Measurement methodology*

(a) Time-resolved PIV. The complex flow structures and intricate instabilities exhibited by swirling flows mandate time-resolved measurements for fundamental insights. The measurement tools can be chosen on the basis of their dynamic response to the fluid flows. The most widely used tools in fluid flows include hot wire anemometry (HWA), laser Doppler anemometry (LDA) and PIV (Adrian 1991; Tropea, Yarin & Foss 2007; Albrecht *et al.* 2013), to name a few. Among these, PIV receives special attention because of its planar measurement features (Sung & Yoo 2001; Schröder *et al.* 2011), unlike LDA and HWA where measurements are pointwise. The arrangement involved in time-resolved PIV is schematically shown in figure 3(*a*,*b*). The arrangement includes a high-speed laser (illumination source) and an imaging system (camera) positioned in an orthogonal manner.

The laser used here is of high-repetition-rate (10 kHz) dual-pulse Nd:YLF type, with a pulse energy of 30 mJ $pulse^{-1}$ at an emission wavelength of 527 nm (make: Photonics Inc.). A flexible guiding arm is employed to direct the cylindrical laser beam towards the measurement section. Furthermore, the cylindrical beam is converted to a thin sheet (∼1 mm) with the help of sheet optics (see figure 3*a*). The focal length f of the sheet optics is chosen as −10 mm, to ensure an optimum aperture angle α to illuminate the desired spatial dimensions of the flow field. In this study, PIV is carried out in two ways. In the first case, PIV is performed only in the gas phase (i.e. without the presence of droplets). In the second case, the flow field in the presence of droplets is imaged. In both cases, only the gas phase is seeded with

https://doi.org/10.1017/jfm.2017.495 Published online by Cambridge University Press

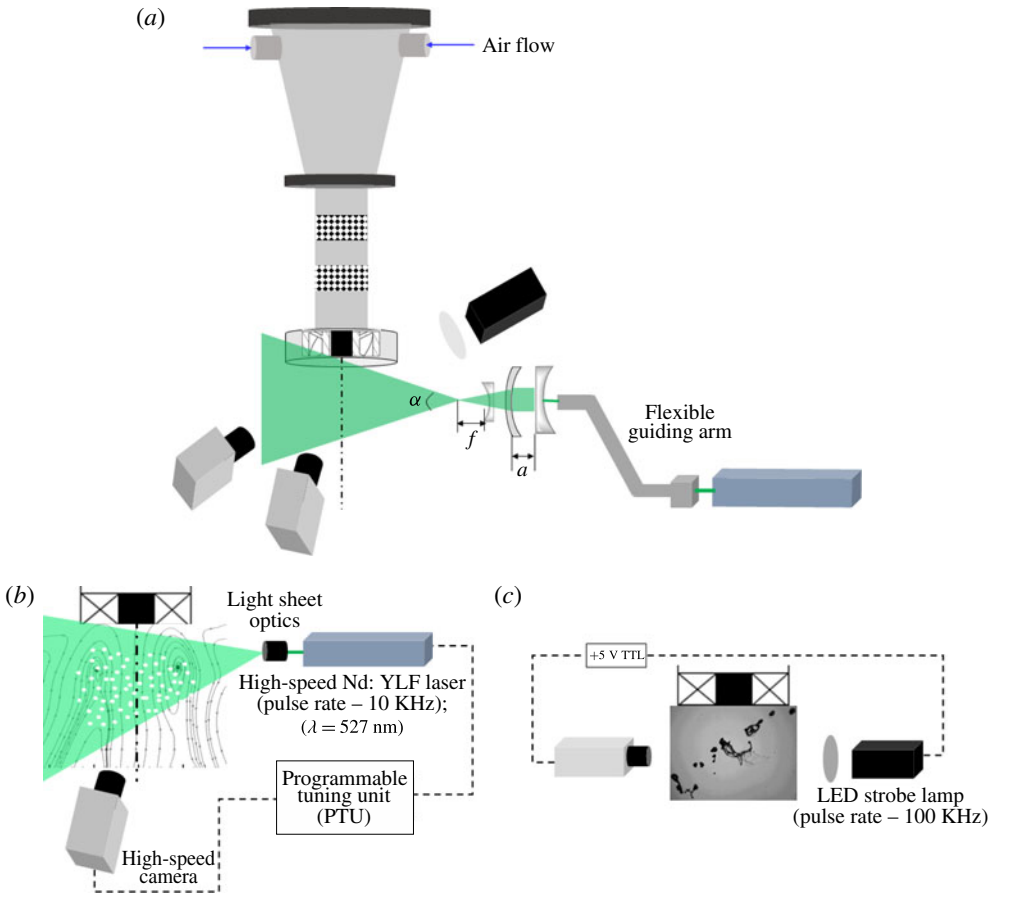

FIGURE 3. (Colour online) (*a*) Schematic showing the arrangement of the different optical diagnostic systems. (*b*) Time-resolved PIV set-up. (*c*) High-speed shadow imaging system.

diethyl hexyl sebacate (DEHS; oil density $\rho = 912$ kg m^{-3}) as tracer particles. The diameter ($\sim$1–3 μm) of tracer particles is chosen in such a way as to maintain tracing accuracy error of less than 1 %. During PIV measurements in the presence of droplets, it is important to minimize the influence of tracer particles in droplet breakup and other related processes (Khalitov & Longmire 2002; Kosiwczuk *et al.* 2005). To validate this, comparison is made between PIV raw images recorded in the presence of both droplets and tracer particles, as well as only with droplets. There is no significant difference in the breakup process, which confirms negligible influence of the tracer particles. In addition, for a given incident laser excitation, the intensity of light scattered by the water droplets is much higher than that by the DEHS particles. This is because the initial size of the injected water droplets ($d_o = 500$ μm) is much higher than that of the DEHS particles ($\sim$1–3 μm), leading to larger scattering cross-sections. This characteristic feature enables to us distinguish the droplets from the DEHS particles in the raw images.

The light scattered by the DEHS particles and droplets is recorded with a Photron SA5 high-speed camera (maximum imaging rate is 7000 frames s^{-1} at 1024 pixel $\times$ 1024 pixel resolution). The camera and laser units are controlled with a programmable

https://doi.org/10.1017/jfm.2017.495 Published online by Cambridge University Press

tuning unit (PTU) to ensure effective synchronization. In addition, an optical bandpass filter of 527 nm is attached in front of the camera lens to avoid any noisy scattering signals due to the ambient. Images are acquired in double-frame mode with an optimal time interval dt between two images. Further details on the steps involved in identifying the optimal dt, tracer particles and other PIV measurement settings can be found in Keane & Adrian (1990) and Raffel *et al.* (2013).

Across all the flow conditions, images are acquired at 3.5 kHz (3500 frames s^{-1}) with an acquisition time of 0.59 s (i.e. 2000 images are acquired for each case). Superior spatial resolution is ensured by employing a magnification factor of ∼10.24 (10 pixels mm^{-1}) with a field of view (FOV) of 100 mm × 100 mm.

The vector fields are reconstructed from the recorded double-frame raw images using a commercial PIV postprocessing package (Davis 8.3; make: Lavision GmbH). The vector field calculation is carried out using a cross-correlation technique with a multipass decreasing window size (the final interrogation window size is 48 pixel × 48 pixel). The choice of interrogation window size (i.e. 48 pixel × 48 pixel) is arrived at based on the peak correlation value (0.8–0.9) inside the field of view.

The accuracy of the PIV measurements is highly dictated by the laser sheet thickness (δ_t), the time delay between two pulses (dt), the particle displacement (δs) and the number of particles (N) per interrogation window. The correctness of the abovementioned parameters is validated by performing uncertainty analysis using the 'correlation statistics' method. This method attempts to compute the disparity between the correlation peaks observed across two images. The uncertainty in the velocity ($\boldsymbol{u}_{error}$) values is computed based on the positional disparity observed across two peaks. In the present study, the uncertainty in the velocity is found to be ±1 % of the local velocity value. Further details about this method can be found in Sciacchitano, Wieneke & Scarano (2013) and Wieneke (2015).

(b) High-speed shadow imaging. The near-field (i.e. locations close to the initial interaction) droplet breakup mechanism and vortex–droplet interactions are visualized using a high-speed shadow imaging system. The optical arrangement involves in the same plane mounting of a high-pulse-rate (100 kHz) LED strobe lamp (make: IDT vision) and a high-speed camera in the same plane (see figure 3*a*,*c*). A diffuser plate is positioned in front of the strobe lamp to ensure uniform background light intensity. Furthermore, the camera shutter and strobe lamp flash duration are synchronized via a delay generator to yield time frozen images of the droplets.

For near-field imaging, a long-distance microscope (make: Questar; QM1 model) with a zoomed-in field of view of 10 mm × 10 mm is coupled to the high-speed camera. This arrangement ensures a relatively high spatial resolution (i.e. magnification factor ∼75 pixels mm^{-1}). Images are acquired at 7500 frames s^{-1} with an exposure time of 1/7500 s. The acquisition time is chosen as 0.67 s (i.e. 5000 images per experimental realization).

2.2. *Flow parameters and test conditions*

The experiments are globally characterized using two major non-dimensional numbers, the liquid and gas phase Reynolds numbers (Re_g, Re_l), and the momentum ratio (MR). These two parameters represent global flow conditions, whereas the local droplet–vortex interaction dynamics is characterized by the Weber number defined based on the vortex strength (We) (to be explained later),

$$Re_g = \frac{\rho_g U_g D_{s,eff}}{\mu_g}, \tag{2.1}$$

https://doi.org/10.1017/jfm.2017.495 Published online by Cambridge University Press

Test case	Airflow rate (lpm)	Liquid flow rate (lpm)	Air Reynolds number (Re_g)	Liquid Reynolds number (Re_l)	Momentum ratio (MR)	Nature of momentum coupling
$C1$	0	0.05	0	675	0	—
$C2$	500	0.05	5 089	675	184	LG–GL
$C3$	1000	0.05	7 965	675	450	G–L
$C4$	1500	0.05	14 177	675	1920	GL
$C5$	2000	0.05	22 874	675	3720	GL
$C6$	2500	0.05	28 805	675	5899	GL
$C7$	3000	0.05	33 888	675	8164	GL

TABLE 1. Experimental test cases.

LG–GL, liquid to gas and gas to liquid two-way coupling; G–L, transition to one-way gas to liquid coupling; GL, strong one-way gas to liquid coupling.

$$Re_l = \frac{\rho_l U_l D_o}{\mu_l}, \tag{2.2}$$

$$MR = \frac{\rho_g U_g^2 A_{s,eff}}{\rho_l U_l^2 A_o}. \tag{2.3}$$

Here, the parameters ρ, μ and U are the density, the viscosity and the bulk exit velocity of the fluids used, where 'g' and 'l' stand for the gas and liquid phases respectively. Since the airflow is routed through the swirler, it is customary to define an effective diameter $D_{s,eff}$ to account for the vanes and hub in the flow path. In most previous works, the area ratio ($A_{s,eff}/A_o$) is not included in the calculation of MR. In those cases, MR is viewed as the dynamic pressure ratio between two coflowing fluids. Few researchers (Engelbert, Hardalupas & Whitelaw 1995; Lozano *et al.* 2005) have explicitly included the area ratio for precise representation of the momentum transfer across the two fluids. For instance, if the area ratio is not included in (2.3), the calculated value of MR for all of the flow cases shown in table 1 is found to be <1, which implies a weak interaction between the droplets and the flow. However, the experimental observations show different trends, i.e. significant coupling (one-way and two-way) for almost all of the airflow rates.

Further, it should be noted that the term U_l in (2.2) is the bulk liquid jet velocity at the nozzle exit before it breaks up into droplets. Here, U_l is evaluated based on the mass conservation principle. In addition, the axis length scales (y, r) are non-dimensionalized with the swirler outer annulus radius (R_o). The experimental flow conditions are compiled in table 1.

3. Global characterization of the flow field using time-resolved PIV

This section describes the global coupling between the swirling gas phase and the droplets injected at various locations across different levels of airflow rates ($0 \leqslant Re_g \leqslant 33\,888$). The flow field signature acquired from time-resolved PIV is elucidated in this section. In the first part, we present the topological modifications of the flow field, including global quantities such as the time-averaged vorticity contours, velocity field and streamlines, among others. Next, we will show how the droplets respond to the vortices (convective and absolute) in the swirling gas flow field. The flow field information presented corresponds to the gas phase with and without droplets.

https://doi.org/10.1017/jfm.2017.495 Published online by Cambridge University Press

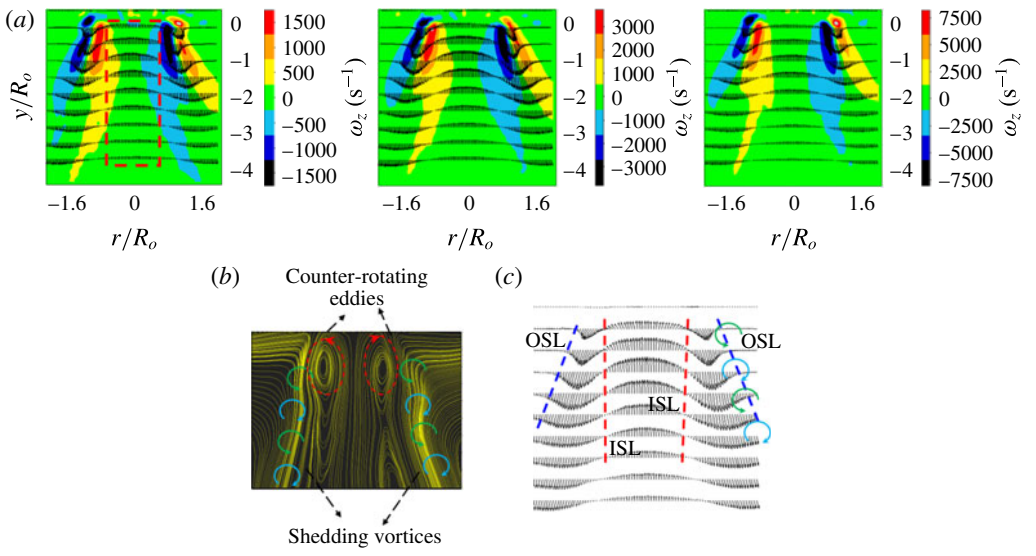

FIGURE 4. (Colour online) The time-averaged flow field without droplets. (*a*) The velocity field superimposed with vorticity contours (without the presence of droplets; *C*2, *C*4, *C*7; $Re_g = 5089, 14\,177, 33\,888$). (*b*) Streamline plot illustrating shedding and counter-rotating vortices. (*c*) Illustration of different forms of shear layers in the velocity field. Adapted from Rajamanickam & Basu (2017).

3.1. *Global swirling flow field in the absence of droplets*

The global features of the flow field are elucidated on the basis of vector fields reconstructed from the PIV raw images. It is mandatory to analyse the gas phase flow field in the absence of droplets across all flow rates since the droplet interaction is expected to be a strong function of *MR*. The time-averaged flow fields obtained for different airflow rates are shown in figure 4. For brevity, only three flow conditions (*C*2, *C*4, *C*7) are shown in figure 4(*a*). The remaining data can be found in the supplementary material (§ 1, figure S1) available at https://doi.org/10.1017/jfm.2017.495. It should be noted that the flow field looks identical in a topological sense for all cases (figure 4), irrespective of airflow rate. This feature can be elucidated by invoking the definition of swirl number (S_G), which embodies the ratio between the axial flux of tangential momentum and the axial flux of axial momentum,

$$S_G = \frac{\int_{R_h}^{R_o} \rho U_y U_w 2\pi r^2 \,\mathrm{d}r}{\int_{R_h}^{R_o} \rho U_y^2 2\pi r \,\mathrm{d}r}. \tag{3.1}$$

Beér & Chigier (1972) showed that for a flat vane swirler, the ratio between the two fluxes (tangential and axial) is geometry-dependent and remains constant irrespective

https://doi.org/10.1017/jfm.2017.495 Published online by Cambridge University Press

of the flow rate. Hence, (3.1) can be rewritten as

$$S_G = \frac{2}{3}\left[\frac{1-\left(\frac{d_h}{d_o}\right)^3}{1-\left(\frac{d_h}{d_o}\right)^2}\right]\tan \emptyset, \tag{3.2}$$

where d_o and d_h are the swirler outer and inner hub diameters.

In the present experiments, the swirl number (S_G) is found to be 0.81, which represents a strong swirling jet (figure 3*b*). Detailed information regarding the spatial regimes of the abovementioned flow configuration can be found in Rajamanickam & Basu (2017).

3.1.1. *Evolution of vortices in the flow field*

The combined action of centrifugal and axial shear instabilities in swirling flow leads to two major forms of vortices (Chigier & Chervinsky 1967; Gallaire & Chomaz 2003). First, vortices are shed in the OSL (see figure 4*b*,*c*) due to the axial shear instabilities with the ambient fluid. Second, the rotational influence of the flow leads to the formation of VBB near the vicinity of the swirler (Billant, Chomaz & Huerre 1998; Champagne & Kromat 2000). Vortex bubble breakdown is identified as the characteristic feature of any flow with rotational influence (Benjamin 1962; Sarpkaya 1971). Hall (1967) reported that the stagnation point in the flow field is the prime cause for vortex breakdown. The stagnation point occurs only when the flow acquires sufficient angular momentum. This criterion translates to a critical value of the swirl number in the current experimental conditions. It has been experimentally validated that vortex breakdown occurs if the swirl number is $\geqslant$0.6 (Lucca-Negro & O'doherty 2001; Liang & Maxworthy 2005). Strong centrifugal instabilities associated with vortex breakdown lead to the formation of a CTRZ characterized by two counter-rotating vortices (see figure 4*b*). Hence, unlike axial round jets, swirling jets exhibit an ISL (figure 4*c*), in addition to the OSL, due to the recirculated flow (see figure 4*c*; see also movie 1). Among these two, the counter-rotating vortices exhibit higher strength, which can be delineated from the vorticity magnitudes shown for all of the cases in figures 4(*a*) and S1.

3.1.2. *Droplet injection locations*

It has already been said that the shear strength and the TKE are the two prime parameters in the context of coaxial atomization. Hence, to identify the optimal injection location, the spatial distributions of these two parameters are evaluated from the vector field calculated from PIV. The procedure involved with calculation of the shear strength from the flow field is shown in the supplementary material. Figure S2*a*,*b* shows that the majority of shear strength and TKE is concentrated in the region $0 < y/R_o \leqslant 1.5$; $-1 < r/R_o < 1$. This is due to the combined azimuthal and axial shear induced by VBB in that region. In addition, the flow recirculation induced by the pressure deficit (due to VBB) causes opposite signs in the radial (U_r) and axial (U_y) velocities (see figure 5*c*,*d*). The flow is subdivided into two spatial regimes, namely zone A and zone B (figure 5*a*). Zone A is essentially a region exhibiting counter-rotating eddies (VBB), while zone B is governed by low-energy shedding eddies.

From the above arguments, it is conceived that the region $0 < y/R_o \leqslant 1.5$ is ideal for droplet injection. Furthermore, in the spatial region $0 < y/R_o \leqslant 1.5$, $1 \leqslant r/R_o \leqslant 1$,

https://doi.org/10.1017/jfm.2017.495 Published online by Cambridge University Press

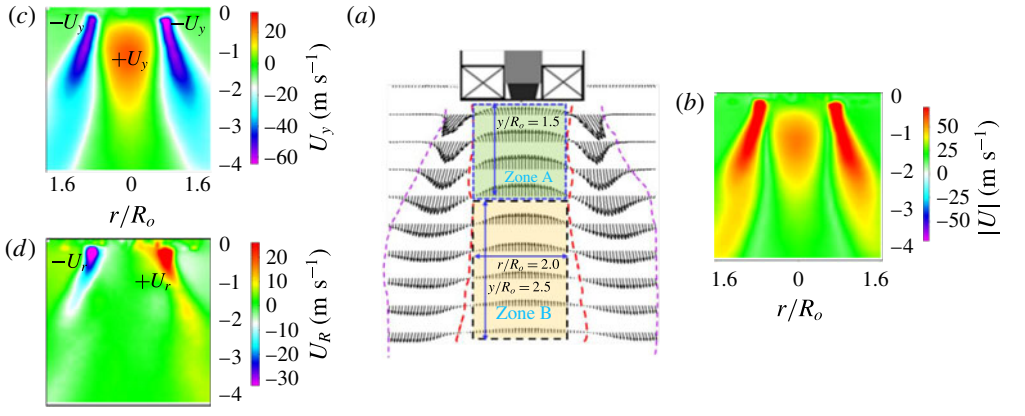

FIGURE 5. (Colour online) Salient features of the swirling gas flow field in the spatial domain: (*a*) time-averaged velocity field; (*b*) time-averaged velocity distribution; (*c*,*d*) time-averaged axial and radial velocity contours. Adapted from Rajamanickam & Basu (2017).

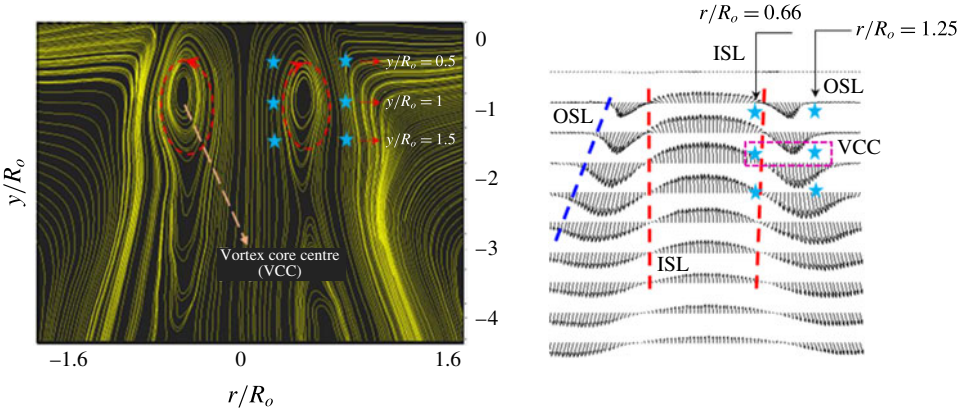

FIGURE 6. (Colour online) Illustration of the droplet injection locations in the swirling gas flow field.

two radial and three axial injection positions are selected, as shown in figure 6. The radial positions (r/R_o) are chosen so as to inject the droplets at the OSL and ISL (see figure 6). In addition, with respect to the core of the vortex breakdown bubble, three axial positions are chosen, the intermediate of which corresponds to the vortex core centre (VCC) ($y/R_o = 1$). The other two positions are chosen at locations upstream ($y/R_o = 0.5$) and downstream of the VCC ($y/R_o = 1.5$) (figure 6). The chosen injection locations (with corresponding acronyms) are summarized in table 2.

3.2. *Global response of the swirling flow field in the presence of droplets*

The alterations of the flow field in the presence of droplets with respect to different injection locations (OSL 1–3, ISL 1–3) are shown in figure 7 and figure S3. To elucidate the topological modifications, the flow field involving only droplets (i.e. $MR = 0$) is also shown in figure 7(*a*). From a global viewpoint, it is seen that at very low airflow rates (i.e. $MR = 185$, $Re_g = 5089$), the injected droplets penetrate inside

https://doi.org/10.1017/jfm.2017.495 Published online by Cambridge University Press

r/R_o location	y/R_o location	Nomenclature	Remarks
	0.5	OSL 1	Upstream of VCC
1.25	1	OSL 2	Centre of VCC
	1.5	OSL 3	Downstream of VCC
	0.5	ISL 1	Upstream of VCC
0.66	1	ISL 2	Centre of VCC
	1.5	ISL 3	Downstream of VCC

TABLE 2. Droplet injection locations.

the vortex core region, which results in complete alteration of the flow field (see the first column in figure 7*b*,*d* and figure S3). In these conditions, substantial momentum is transferred from the liquid to the gas phase, leading to flow variations. On the other hand, slight variation is observed in the droplet trajectories (shown later), without any major breakup event. This situation represents two-way coupling between the droplets and the swirling gas phase (denoted as LG–GL coupling (i.e. liquid to gas, gas to liquid)). However, at high airflow rates ($14\,000 < Re_g \leqslant 33\,888$, $1920 < MR \leqslant 8164$), the swirling gas flow predominantly transfers momentum to the liquid droplets, leading to different forms of breakup and dispersion (to be explained later). Here, the flow field (see the second and third columns in figure 7*b*,*d*) resembles the one shown in figure 3(*a*). This is identified as one-way gas to liquid coupling (GL coupling). Hence, with the increase in the airflow rate, a transition is observed from two-way LG–GL to one-way GL coupling. This G–L coupling transition occurs at ($Re_g \sim 7965$, $MR \sim 450$), where the effect of droplets on the flow field starts to become insignificant in a global sense.

The gas phase flow fields for OSL and ISL injection are largely unaltered for high MR, except that there is slight deformation of the vortex core in certain local regions (shown as white dotted lines in figure 7*b*i,ii). On account of this, slight change in orientation is observed for the vector fields (see figure 7*c*). In particular, for injections corresponding to upstream of the vortex core (OSL 1), significant alteration of the vector field is detected. For instance, the deviation angle α subtended by the velocity vectors for OSL 1 ($y/R_o = 0.5$) (figure 7*c*) is found to be as high as 39°. Interestingly, the vector field deformation is much more pronounced in the recirculation zone (VBB). For these injection locations (OSL 1, OSL 2), the vortex core rotation is abruptly disturbed, leading to change in the orientation of the flow direction. This effect is not observed for the $y/R_o = 1.5$ location, because of the downstream nature of the injection (i.e. position away from the vortex core); in essence, the vortex core experiences negligible impact from the injected droplets (figure 7*b*,*c*). In addition, the vortex core remains unaltered for all injection locations at the ISL. This yields a similar flow field irrespective of the injection location (ISL 1–3). Hence, in figure 7(*d*), only the flow field pertaining to ISL 1 is shown; the others (ISL 2, 3) can be found in figure S3(ii),(iii).

The fundamental response between the gas phase vortices and the liquid droplets can be explained by a simple force balance model (see figure 8*a*). The parameter ξ, which defines the dynamic pressure ratio between the two phases (3.3) is used as a criterion to understand this phenomenon. The dynamic pressure ratio ξ is the parameter that quantifies momentum transfer pathways between two coflowing fluids. For example, in situations where $\xi < 1$, (3.3) represents the momentum transfer occurring from the liquid to the gas phase (i.e. LG coupling). The airflow rate

https://doi.org/10.1017/jfm.2017.495 Published online by Cambridge University Press

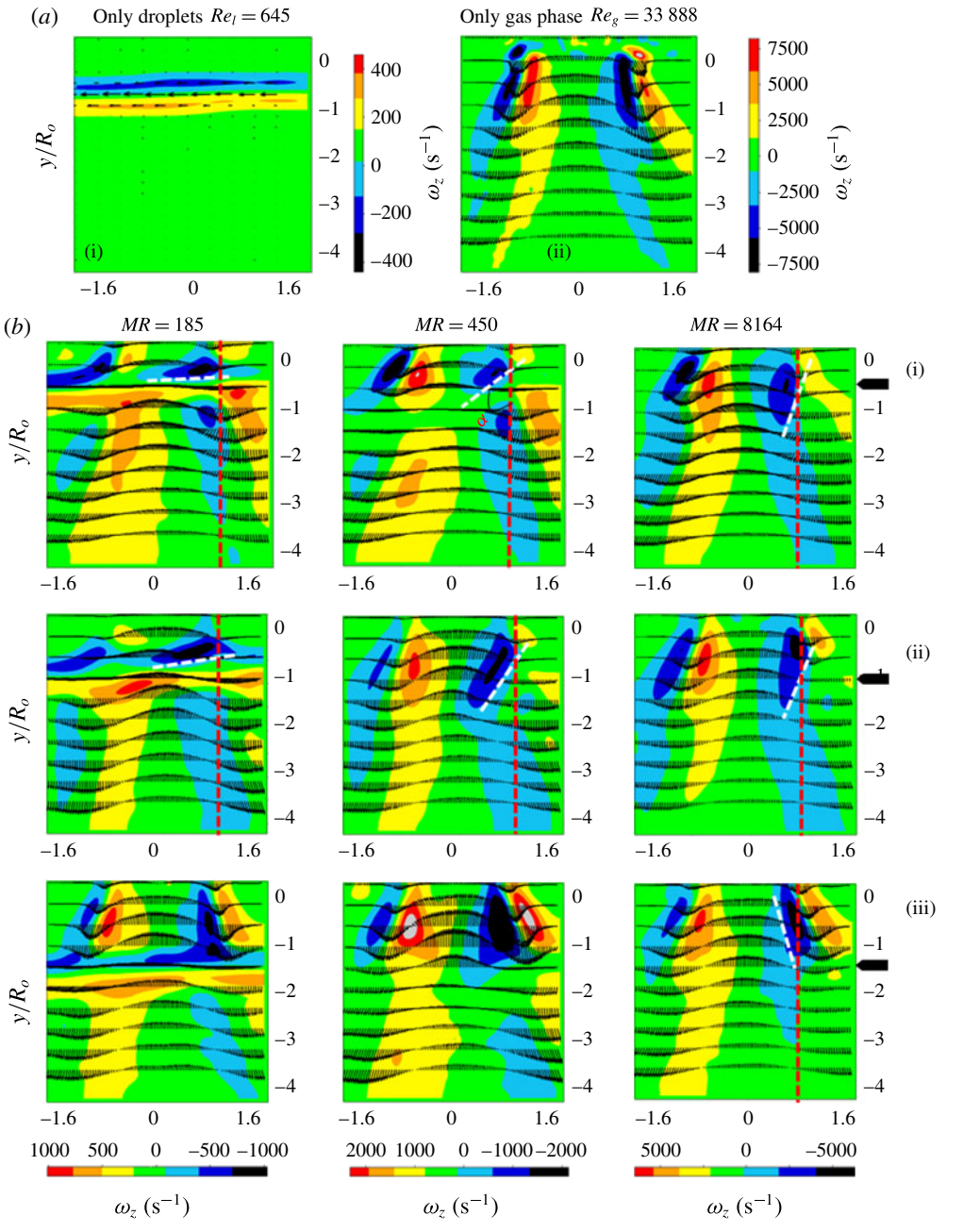

FIGURE 7. For caption see next page.

pertaining to $\xi \sim 1$ is delineated as the transition condition, followed by strong one-way gas phase coupling when $\xi \gg 1$ (i.e. GL coupling).

$$\xi \sim \frac{\rho_a (V_\omega)^2}{\rho_l (V_d)^2}. \tag{3.3}$$

https://doi.org/10.1017/jfm.2017.495 Published online by Cambridge University Press

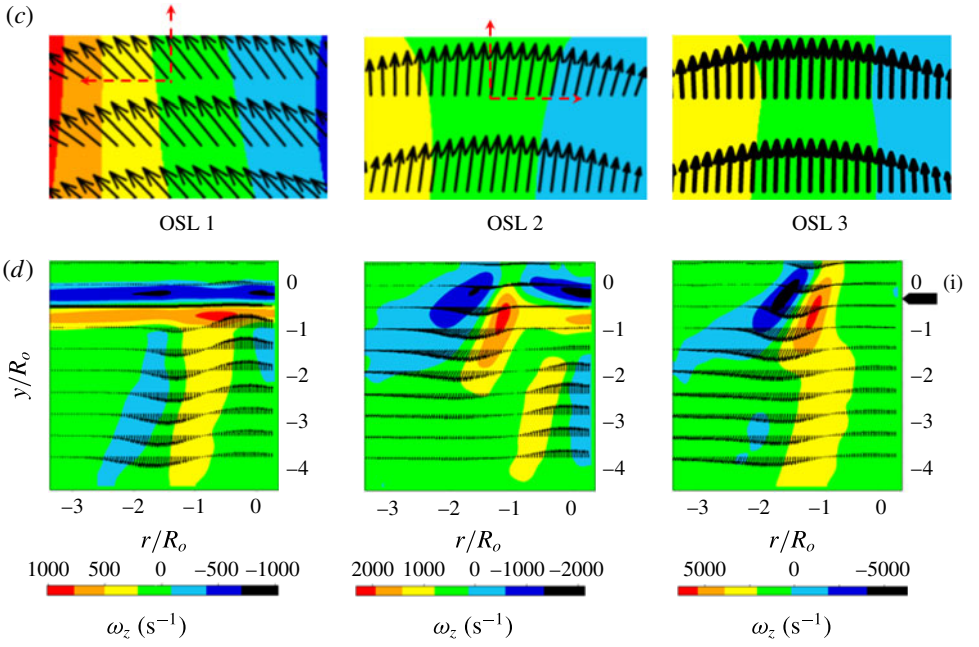

FIGURE 7. (cntd). (Colour online) Illustration of the global evolution of the flow field (time-averaged). (*a*) The flow field for only the liquid phase and the gas phase. (*b*,*d*) The combined liquid and gas phase flow field for droplets injected at the OSL and the ISL: (i) OSL 1, ISL 1; (ii) OSL 2; (iii) OSL 3. (*c*) The deformation of the vector field (with respect to the gas phase flow field in figure 4*a*) near the vortex core region for OSL injection.

Here, V_ω represents the velocity induced by vortices. It can be written in terms of the space–time-averaged circulation strength ($\overline{\Gamma}$) as $V_\omega = \overline{\Gamma}/2\pi r$, where r is the vortex core radius, which is calculated from a time-averaged streamline plot obtained from PIV. The steps involved in calculation of the circulation strength $\overline{\Gamma}$ from the vorticity magnitude will be explained later in great detail. The droplet velocity V_d is acquired from PIV without coflowing swirl air (i.e. $MR = 0$). For $0 < Re_g < 7164$, the value of ξ is found to be less than 1, which shows that the effect of $\overline{\Gamma}$ is minimal and injected droplets penetrate inside the vortex core (figure 8*b*). On the other hand, increased circulation strength $\overline{\Gamma}$ at $7164 \leqslant Re_g \leqslant 33\,888$ causes $\xi \gg 1$, which acts as a barrier to droplet penetration. As mentioned earlier, the deflection caused to the vortex eye for $x/R_o = 2.5$ (OSL) is due to direct impact of droplets on the vortex centre (figure 8*c*). However, the opposite effect is observed for $x/R_o = 0.7$ (ISL); here, the injected droplets first interact with the recirculation zone, resulting in upward motion of the droplets. This phenomenon prevents direct impact of droplets on the right side of the vortex core, resulting in a virtually unaltered flow field (figure 8*d*).

Since, in these experiments, the liquid phase flow rate is maintained constant, the only variable that governs the dynamic pressure ratio ξ is the circulation strength of the vortex (i.e. $= f(\overline{\Gamma})$). Hence, the control parameter that defines this global modification is $\overline{\Gamma}$. The circulation strength $\overline{\Gamma}$ corresponding to the transition flow condition ($Re_g \sim 7965$, $MR \sim 450$) is identified as critical $\overline{\Gamma}_c$.

https://doi.org/10.1017/jfm.2017.495 Published online by Cambridge University Press

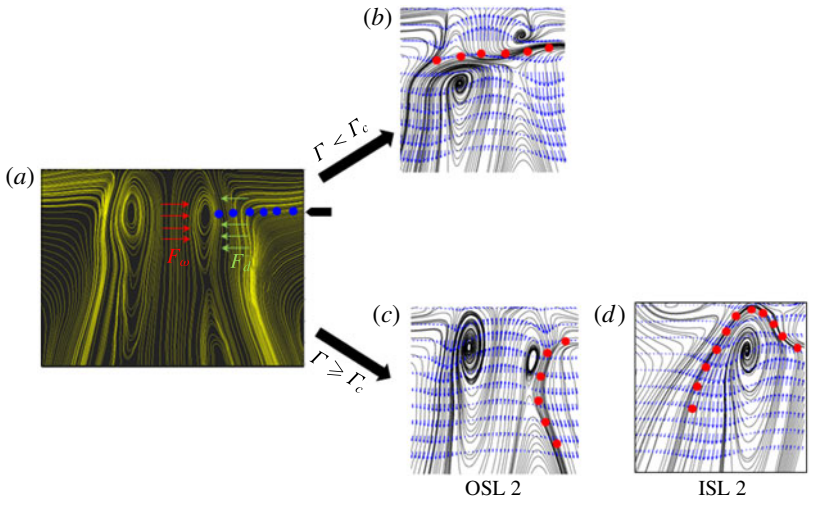

FIGURE 8. (Colour online) Global representation of droplet response with vortices. (*a*) Diagram illustrating the forces between the vortices and the droplets. (*b*) The vortex–droplet interaction at $MR = 0$. (*c*,*d*) The vortex–droplet interactions at high airflow rates ($MR = 8164$).

3.3. *Global response of droplets in the swirling gas flow field*

The results shown in the previous section outline how the global flow field is modified in the presence of the droplets. Here, we describe how the droplets respond to the swirling flow field (at both the OSL and the ISL). Once again, the results shown here are intended only for quantifying the global parameters. The detailed droplet–vortex interaction and breakup dynamics will be explained later using a high-speed shadow imaging technique.

To illustrate the dynamics, only droplet images are extracted from the PIV raw images, and the image processing steps involved with this are shown in figure S4.

The global response of the droplets on interaction with the vortical structures is shown in figure 9. Here, only two extreme cases are shown (i.e. one for OSL and the other for ISL injection, i.e. OSL 2 and ISL 2) across three flow conditions ($MR = 185$, 450, 8164). From the droplet perspective, the acquired images show LG–GL coupling ($MR = 185$) with the vortex (see figure 9ii). The droplet pathways are altered but not in a significant fashion. Similarly, in transition flow conditions ($MR \sim 450$), the increased circulation strength imposed by the vortex results in a strong interaction between the droplet and the swirling flow field (G–L). As a result, the droplet trajectory deviates from its straight path by an angle θ' (spatially averaged instantaneous angle, shown as red dotted lines in figure 9iii–vi) along with significant spatial dispersion (explained in detail in later sections). The magnitude of the dispersion increases with the momentum ratio (MR), as evidenced in figure 9(iv) and (vi). The global observations can be summarized as follows:

(1) $0 < Re_g < 7164, 0 < MR < 450 \rightarrow \overline{\Gamma} < \overline{\Gamma}_c \rightarrow$ two-way LG, GL coupling (movie 2);
(2) $Re_g \approx 7164, MR \approx 450 \rightarrow \overline{\Gamma} \sim \overline{\Gamma}_c \rightarrow$ transition to one-way GL coupling (movie 3);
(3) $7164 \leqslant Re_g \leqslant 33\,888, 450 \leqslant MR \leqslant 8164 \rightarrow \overline{\Gamma} \geqslant \overline{\Gamma}_c \rightarrow$ strong one-way GL coupling (movie 4).

https://doi.org/10.1017/jfm.2017.495 Published online by Cambridge University Press

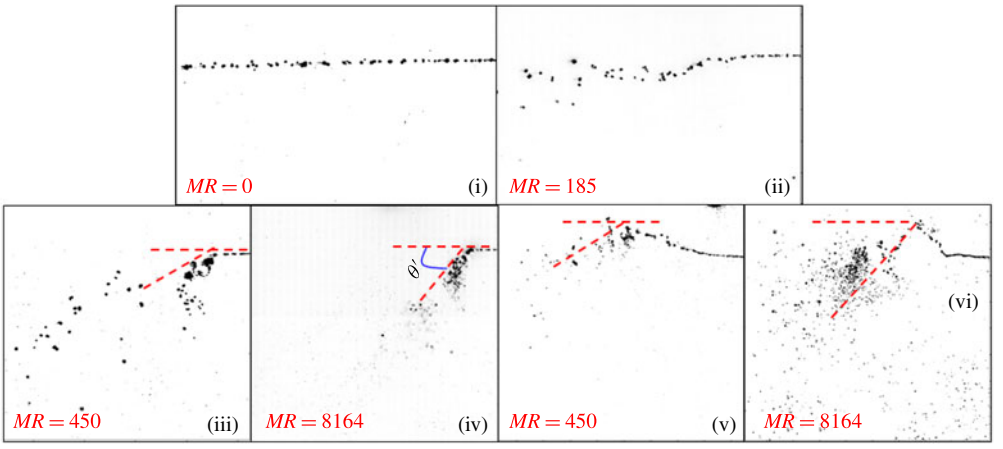

FIGURE 9. (Colour online) Sample instantaneous visualization of droplet trajectories: (i), (ii) droplet trajectories at low MR; (iii), (iv) droplets injected at the OSL (OSL 2) at medium to high MR; (v), (vi) droplets injected at the ISL (ISL 2) at medium to high MR.

To precisely locate the transition, experiments were carried out for three to four flow rates ($MR = 365$, 402, 420) close to the transition state. Strictly speaking, the transition does not pertain to a particular value, rather it is observed over a range. In the present experiments, we observed the transition in the range of $420 \leqslant MR \leqslant 460$. However, for simplicity we have considered $MR \sim 450$ as a representative critical/transition flow condition.

In a nutshell, $\overline{\Gamma}$ is the forcing parameter induced by the vortex strength, which will predominantly determine the global response θ' of the droplet. The absolute values for $\overline{\Gamma}$ and θ' will be shown in later sections.

4. Flow–droplet interaction dynamics

We will now look into the interaction dynamics between the instantaneous circulation (rather than averaged circulation) strength Γ' and the dispersion angle θ'. It is well known that the swirling flow field will exhibit fluctuations in the circulation strength Γ' which in turn introduce dynamical behaviour (modes of breakup and spatial dispersion) in the droplets that cannot be deciphered using $\overline{\Gamma}$. Hence, in this section, the idea is to extract the instantaneous circulation strength (Γ') and dispersion angle (θ') and quantify the dynamic coupling between Γ' and θ' using spectral coherence analysis $\{C_{\Gamma'\theta'}(f)\}$. The procedure involved in the computation of Γ' and θ' from high-speed simultaneous PIV raw images is shown in figure S5 (§ 2.2 in the supplementary material). Here, the dispersion angle θ has two forms; one pertains to the mean angle (spatial sense) observed at any given instant of time (i.e. θ') and the second is the space–time-averaged dispersion angle ($\overline{\theta}$).

4.1. *Coherence analysis*

The essential role of coherence analysis is to estimate the relationship between the input $x(t)$ and output $y(t)$ signal in a linear time invariant system. Mathematically, it is defined as the ratio between the cross-spectral density of $x(t)$, $y(t)$ and the auto

https://doi.org/10.1017/jfm.2017.495 Published online by Cambridge University Press

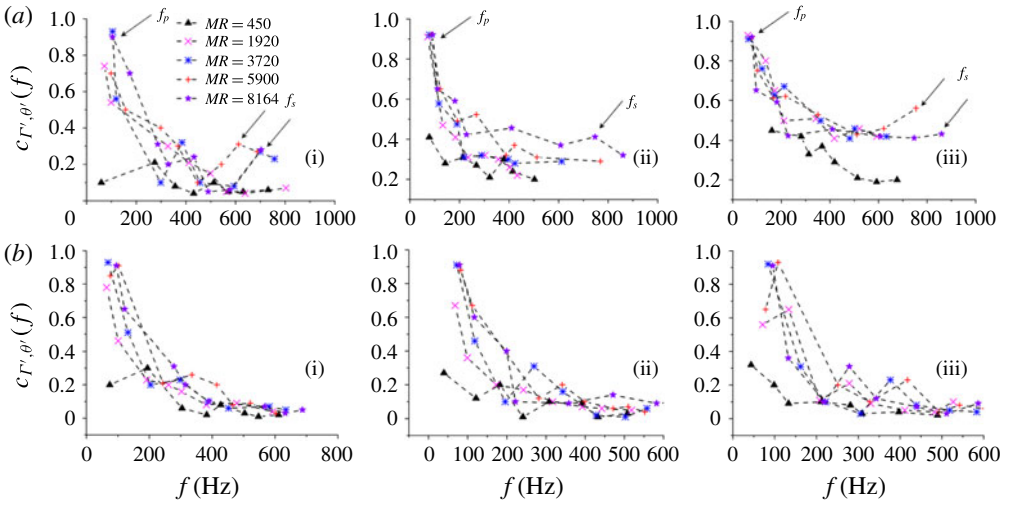

FIGURE 10. (Colour online) The coherence function $C_{\Gamma',\theta'}(f)$ (*a*) evaluated for droplets injected at the OSL and (*b*) evaluated for droplets injected at the ISL: (i) OSL 1, ISL 1; (ii) OSL 2, ISL 2; (iii) OSL 3, ISL 3.

spectral density of $x(t)$, $y(t)$ (Bendat & Piersol 1980). The coherence value can vary from 0 to 1; the higher the coherence value is (i.e. closer to unity), the greater the chance of linearity between the two signals:

$$C_{x,y}(f) = \left\{ \frac{|G_{xy}(f)|^2}{G_{xx}(f) \cdot G_{yy}(f)} \right\}, \quad 0 < C_{x,y}(f) < 1. \tag{4.1}$$

In the present experiments, $x(t)$ and $y(t)$ are Γ' and θ' respectively; hence, equation (4.1) can be written as

$$C_{\Gamma',\theta'}(f) = \left\{ \frac{|G_{\Gamma'\theta'}(f)|^2}{G_{\Gamma'\Gamma'}(f) \cdot G_{\theta'\theta'}(f)} \right\}. \tag{4.2}$$

The coherence function $C_{\Gamma',\theta'}(f)$ evaluated for different injection locations across various flow rates is presented in figure 10. On account of the LG–GL interaction (mostly liquid to flow), coherence values $C_{\Gamma',\theta'}(f)$ are not evaluated for $0 < MR < 450$. The results pertaining to $MR > 450$ are depicted in figure 10(*a*) for droplets injected at the OSL. It is seen that for all three axial positions, higher coherence ($\sim$0.85) is observed around 80–100 Hz. Although the coherence value decays drastically at higher frequencies, interestingly, there is a second peak in $C_{\Gamma',\theta'}(f)$ for frequencies around 600–900 Hz. In particular, these values are higher for downstream injection locations (i.e. OSL 3; figure 10*a*iii). This indicates that the interaction between Γ' and θ' in the OSL (for OSL injections described earlier) is coupled in two frequency bands, namely the primary (f_p) and secondary (f_s).

On the contrary, the dispersion of droplets injected at the ISL (figure 10*b*; ISL injections) is predominantly coupled with the local circulation in a narrow frequency band (80–100 Hz) exhibiting very high coherence values of $\sim$0.85–0.9. These two contradictory behaviours between the OSL and the ISL indicate radical changes in the interaction dynamics. In both cases (OSL and ISL injections), the transition flow condition is coupled only in a single frequency range (no second peak) and also exhibits low coherence, $C_{\Gamma',\theta'}(f) \sim 0.2$–025 (figure 10*a*,*b*i).

https://doi.org/10.1017/jfm.2017.495 Published online by Cambridge University Press

5. Proper orthogonal decomposition

The coherence analysis presented in § 4 yields information about the interaction dynamics of vortices and droplets in a swirling gas flow field. The observations made open up avenues for two important questions. First, what is the source of the high coherence at 80–100 Hz? Next, why do the droplets (i.e. trajectories) at the OSL couple with the flow field at multiple frequency bands compared with the ISL droplets? To understand the source of the frequencies observed in the vortex–droplet interaction, it is necessary to identify the dominant instability mechanisms that govern the flow field. The instability mechanism and its characteristic frequencies can be extracted in several ways like linear stability analysis, POD and dynamic mode decomposition, among others. In this study, POD is carried out to extract the dominant spatial and temporal modes. Implementation of POD in the flow field enables delineation of the characteristic frequencies of the fluctuating components of the flow field from its temporal modes.

5.1. *Spatial eigenmodes of the gas flow field*

Proper orthogonal decomposition can be implemented in two ways, classical POD and the method of snapshots (Sirovich 1987). The latter one has received greater attention in analysing turbulent flows (Berkooz, Holmes & Lumley 1993). Mathematically, POD decomposes the fluctuation in velocity components (u', v') into spatial (x) and temporal (j) modes. The detailed steps pertaining to implementation of POD over the flow field data are illustrated in figure S6 (§ 2.3).

The spatial eigenmodes $\phi_n(x)$ pertaining to only the gas phase flow field (without droplets) are shown in figure 11. Here, only two flow conditions are shown for brevity, one for low airflow rate ($Re_g = 5089$) and the other for high airflow rate ($Re_g = 33\,888$). It should be noted that the eigenmodes depicted for both airflow rates look identical in the topological sense, due to the fixed value of the swirl number (as explained earlier in § 2). Logically, in POD, the number of eigenmodes is equal to the number of snapshots provided as input. However, only the first few modes contribute towards the overall TKE of the flow field. In the present experiments, the cumulative energy of first four modes (A1–A4) is found to be more than 95 % (see figure 11*c*). Hence, only those eigenmodes are shown in figure 11(*a*,*b*).

Several studies (Billant *et al.* 1998; Gallaire & Chomaz 2003) have reported the dominance of centrifugal or azimuthal shear instabilities in strongly swirling jets ($S_G \geqslant 0.6$). The mechanism/type of the instabilities can be identified with the help of vorticity contours (spatial eigenmodes) and the frequency signatures (see figure 12) extracted from the temporal modes. From the viewpoint of the vorticity distribution along the longitudinal axis (y/r_o), the instability waves can be delineated as symmetric or asymmetric. For instance, modes 1 and 2 exhibit symmetric vorticity distributions (figure 11*a*,*b*A1,A2). Modes 3 and 4 exhibit asymmetric (i.e. helical; figure 11*a*,*b*A3,A4) vorticity distributions.

The strong negative vorticity region observed in the central region of mode 1 (A1) is induced by VBB due to the intense rotation of the fluid in the azimuthal direction (i.e. strong swirling jet, $S_G \geqslant 0.6$). Moreover, in this region, the radial velocity magnitude shows dominance over the axial component ($\partial U_y/\partial r < \partial U_r/\partial y$). This results in a combination of axial and azimuthal shear.

Coles (1965) formulated the criteria for centrifugally unstable flows, which state that the flow becomes locally unstable if the vorticity magnitude in that region is negative (see (5.1)),

$$\omega_z \Omega < 0. \tag{5.1}$$

https://doi.org/10.1017/jfm.2017.495 Published online by Cambridge University Press

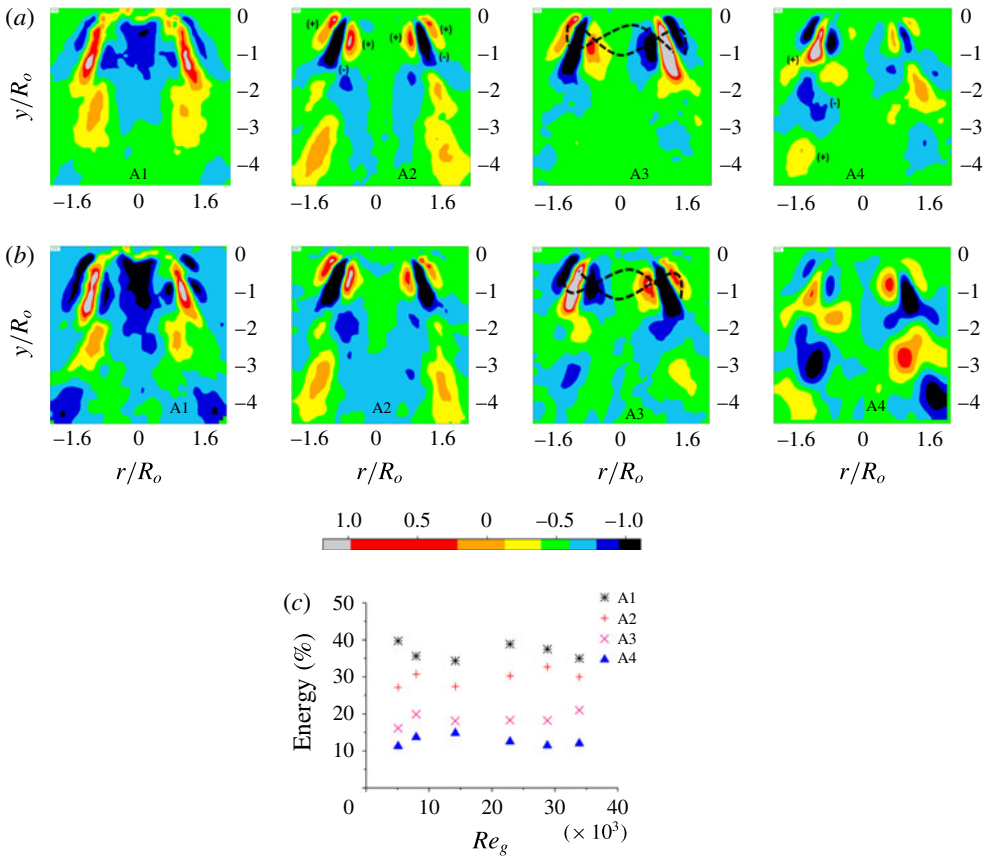

FIGURE 11. (Colour online) (*a*,*b*) Illustration of the POD spatial eigenmodes for only the gas phase for (*a*) $Re_g = 5089$ and (*b*) $Re_g = 33\,888$. (*c*) The modal energy distribution. A1, first mode, KH instability/centrifugal instability; A2, second mode, KH instability/axial shear instability; A3, third mode, helical instability; A4, fourth mode, shedding mode. Adapted from Rajamanickam & Basu (2017).

The dominance of azimuthal and axial shear in modes 1 and 2 is identified as the KH/strong shear instability mode. From the modal energy distribution viewpoint, it can be inferred that the flow field is dominated by azimuthal and axial shear instabilities (A1, A2) which account for 80 % of the total TKE. In contrast, modes 3 and 4 account for only 20 % of the energy.

In general, swirling jets exhibit helical waves before vortex breakdown occurs. This condition is true only for weak swirling jets (i.e. $S_G < 0.6$). However, in this study, the flow condition pertains to a strong VBB state. Hence, the helical modes appear as low-energy-content modes (∼20 % of the total energy). It is important to note that the vorticity contours in the POD modes (in particular for A1, A2 and A3; figure 11*a*,*b*) predominantly appear in the region where counter-rotating vortices are present, whereas only in the fourth mode (A4; low-energy-content mode) do the vortices appear in alternate fashion in the OSL region (figure 11*a*,*b*,A4). The above observations clearly demonstrate the dominance of counter-rotating vortices over shedding vortices (only in the A4 mode). The origin of the shedding vortices

https://doi.org/10.1017/jfm.2017.495 Published online by Cambridge University Press

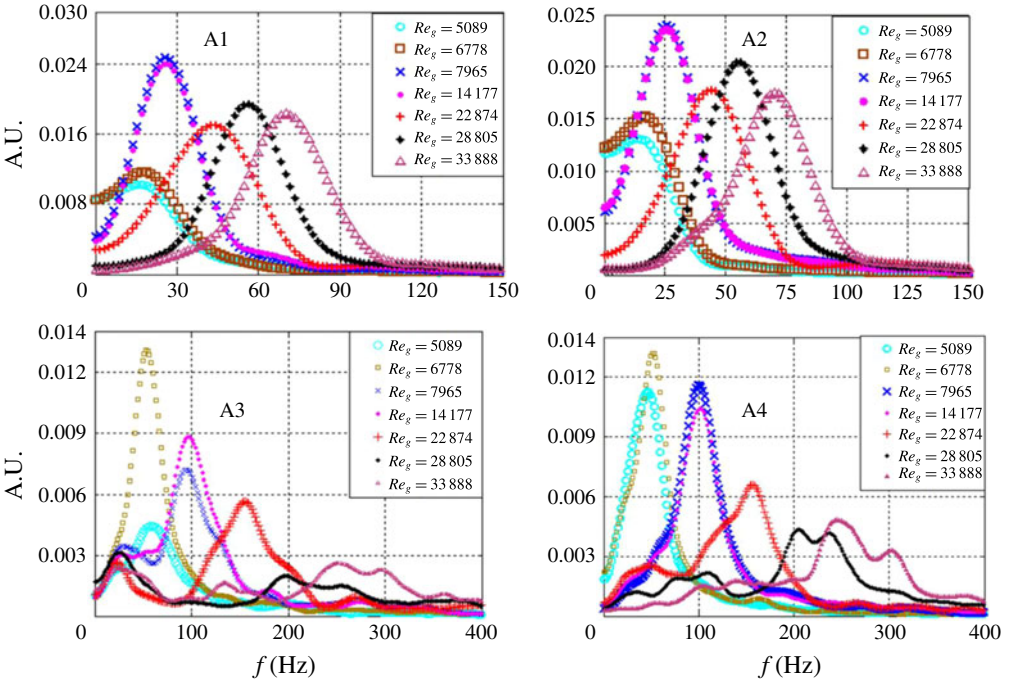

FIGURE 12. (Colour online) Illustration of frequency spectra obtained from the POD temporal modes for only the swirling gas flow field. Adapted from Rajamanickam & Basu (2017).

in the swirl flow can be traced to the oscillations induced by the PVC (Syred 2006; Martinelli, Olivani & Coghe 2007).

The frequency spectra obtained for modes 1 (A1) and 2 (A2) exhibit very narrow bands (see figure 12). The frequency values show an increasing trend with the flow rates from 30 Hz to 75 Hz for A1 and A2. However, repetitive frequency peaks are observed for the helical and shedding modes (A3, A4; figure 12). The important conclusion evident from the frequency signature is the nature of the instability wave induced in each mode. For instance, the single large peak observed around ∼75 Hz for A1 and A2 suggests long waves (i.e. the wavelength is relatively larger than those of modes 3 (A3) and 4 (A4) (i.e. $\lambda_{1,2} > \lambda_{3,4}$)). Since, A1 and A2 are identified as KH instability modes, the frequency signature and wavelength scales pertaining to A1 and A2 are delineated as $f_{1,2} \approx f_{KH}$ and $\lambda_{1,2} \approx \lambda_{KH}$ respectively. Therefore, the frequency signatures in A1 and A2 are mainly contributed by large-scale coherence structures. On the other hand, small-scale/shedding eddies lead to the formation of multiple frequency peaks in A3 and A4. This may due to the coupling of large-scale coherent structures with low-energy-content eddies (i.e. small scale).

5.2. *Spatial eigenmodes in the presence of droplets*

The dominant instability mechanisms that govern the swirling flow field are presented in § 4.2. The objective of this section is to outline the qualitative and quantitative comparisons between the POD spatial eigenmodes pertaining to the flow field with and without droplets. The quantitative information involves coherence analysis between the

https://doi.org/10.1017/jfm.2017.495 Published online by Cambridge University Press

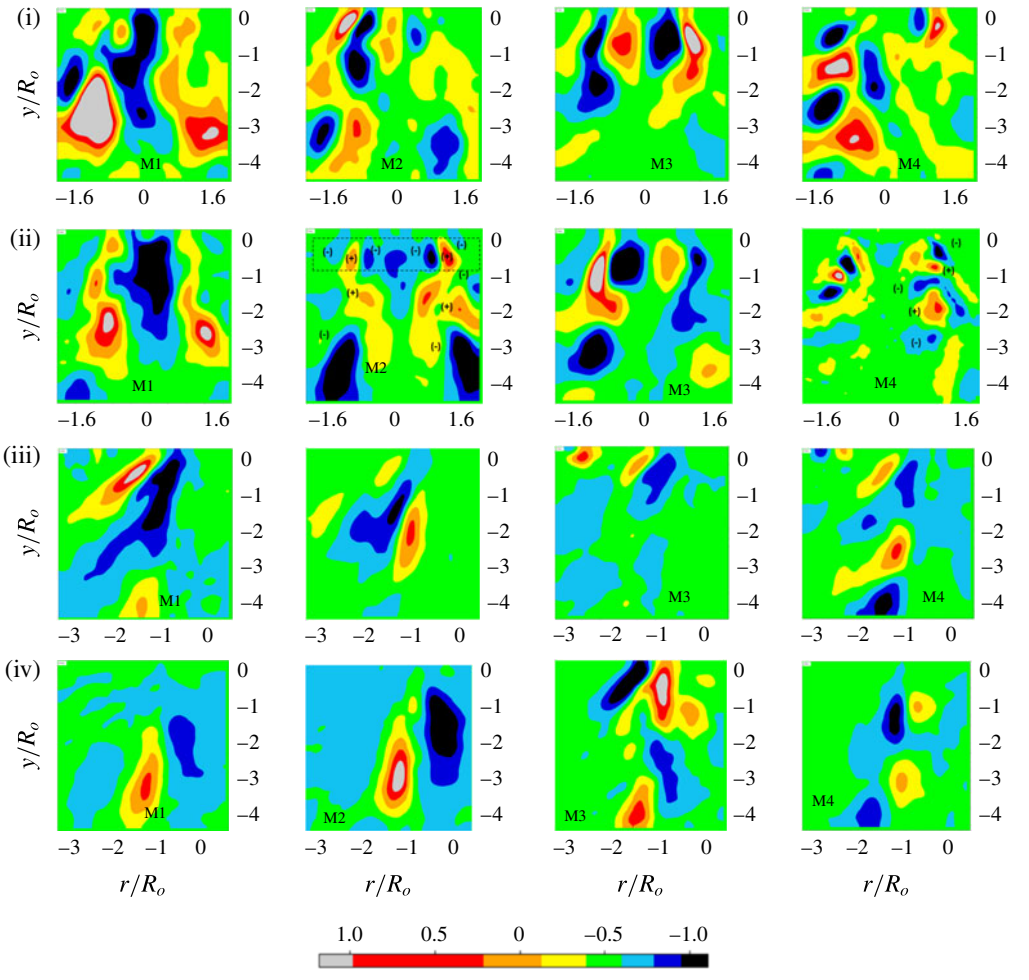

FIGURE 13. (Colour online) The POD spatial eigenmodes computed from the instantaneous swirling gas flow field in the presence of droplets ($MR \sim 8164$): (*a*) OSL 1; (*b*) OSL 2; (*c*) ISL 1; (*d*) ISL 2.

temporal modes and the instantaneous spatially averaged circulation Γ'. This approach reveals the mechanisms behind the modal coupling between the two phases and the corresponding trends in the coherence function $C_{\Gamma',\theta'}(f)$, as observed in figure 10. Since the main interest lies in identifying the instability mechanism involved during strong interaction, only flow rates corresponding to GL coupling ($Re_g \sim 33\,888$, $MR \sim 8164$) are considered here for brevity.

Spatial eigenmodes evaluated from instantaneous vector fields involving droplets for two injection locations (OSL 1, 2; ISL 1, 2) are shown in figure 13. The modal contours pertaining to the flow field with droplets are marked as M1–M4. The contour maps of the spatial eigenmodes suggest strong coupling of the azimuthal shear modes (i.e. M1 and A1 shown in figures 11 and 13 are similar) for both OSL and ISL injections.

The fundamental difference observed in the eigenmodes between ISL and OSL injections is the appearance of secondary instability modes in the OSL case.

https://doi.org/10.1017/jfm.2017.495 Published online by Cambridge University Press

For instance, mode 2 (M2) shown in figure 13(*b*) exhibits shedding as a secondary mode in addition to the shear mode (here, the shear mode is depicted inside the dotted black box) observed in the gas phase. The same observation is valid for M3 also, i.e. the appearance of a shedding mode in addition to the helical modes. In contrast, the ISL depicts only shear (i.e. azimuthal and axial shear) instabilities in the first two modes (see M1 and M2 in figure 13*c*,*d*). The spatial eigenmodes quantified at downstream injection locations (OSL 3, ISL 3) also exhibit similar trends; hence, for brevity, these are shown in the supplementary material (figure S7i,ii).

It should be noted that in figure 12, the helical and shedding modes exhibit multiple frequency peaks. The coupling of secondary modes with highly energetic modes (i.e. M2) in the OSL is suspected to be a cause of the secondary frequencies (f_s) observed in the coherence analysis (figure 10*a*i–iii). To confirm this phenomenon, coherence analysis is carried out between the temporal modes ($a_n(t)$) and the forcing parameter Γ':

$$C_{a_n(t),\Gamma'}(f) = \left\{ \frac{|G_{\Gamma' a_n(t)}(f)|^2}{G_{\Gamma'\Gamma'}(f) \cdot G_{a_n(t)a_n(t)}(f)} \right\}. \tag{5.2}$$

The coherence analysis carried out as per (5.2) is graphically shown in figure 14. Again, the results are shown only for the strong-interaction (GL) case ($Re_g \sim 33\,888$, $MR \sim 8164$). For OSL injection (figure 14*a*–*c*), it is seen that modes M1 and M2 become coupled with Γ' at very high coherence values of 0.8–0.9 in very narrow frequency band (90–110 Hz). In addition, mode 2 (M2, axial shear instability) shows intermediate coherence values of 0.3–0.5 at secondary frequency levels of 300–600 Hz. The interesting point to note in OSL injection is the activation of shedding modes (high-frequency modes) for downstream injection points in combination with high-energy-content modes, i.e. mode 2 (figure 14*b*,*c*). This may be due to interaction of the droplets with shedding vortices (small-scale eddies). Moreover, the instantaneous raw images also suggest predominant interaction of droplets with these shedding vortices (see figure S8*a* and movie 4). Helical and shedding modes (M3 and M4) are coupled in higher and wider frequency bands (200–600 Hz) with lower coherence values. The existence of these secondary frequency bands was already established in the coherence analysis (§ 4) made between Γ' and θ' (see figure 10*a*).

On the contrary, in ISL injection, the droplets undergo breakup (see the blue dotted lines in figure S8*b*,*c*) before they reach the rotating eddies. This pre-breakup of droplets induces a drastic reduction in size, which ultimately leads to lower local Stokes number (see (7.5)) values. The lower Stokes number causes significant droplet trapping inside the vortex core, rather than the interaction with the shedding eddies as observed in the OSL. Modal coherence results for the ISL cases confirmed that the instantaneous circulation values Γ' are primarily coupled with only azimuthal and axial shear instability modes (M1 and M2; see figure 14*d*–*f*), which results in high coherence values of 0.8–0.9 around 80–110 Hz. In both cases (OSL, ISL), the frequency spectra corresponding to KH instability modes are delineated as (f_{KH}).

The coherence observations made in §§ 4 and 5 can be summarized as follows.

For the OSL,

$$\left.\begin{array}{l} \dfrac{x}{R_o} \sim 2.5, \quad \dfrac{y}{R_o} \leqslant 0.7, \quad \text{OSL } 1 \rightarrow \text{ KH mode,} \\ \dfrac{x}{R_o} \sim 2.5, \quad 0.7 \leqslant \dfrac{y}{R_o} \leqslant 1.5, \quad \text{OSL } 2, 3 \rightarrow \text{KH mode + shedding mode.} \end{array}\right\} \tag{5.3}$$

https://doi.org/10.1017/jfm.2017.495 Published online by Cambridge University Press

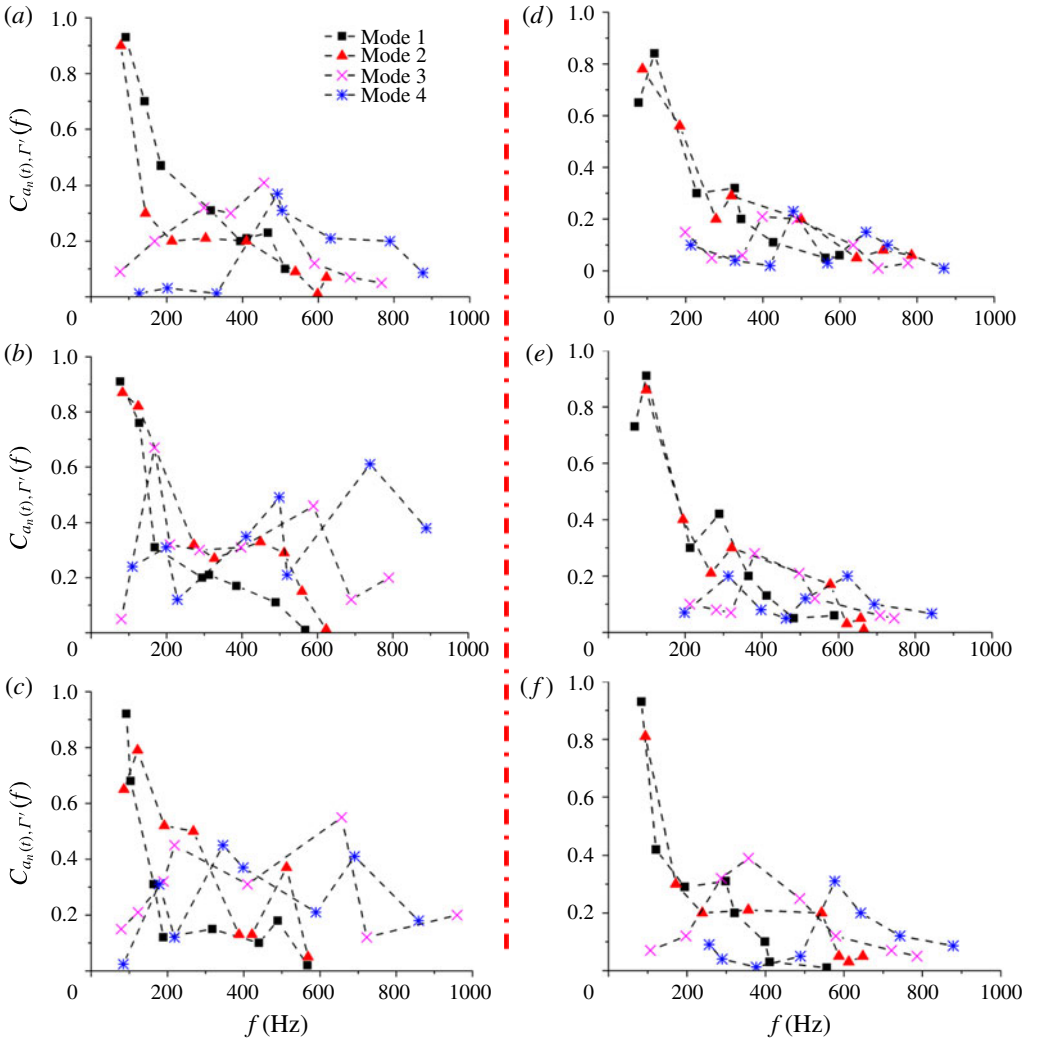

FIGURE 14. (Colour online) Coherence plots illustrating the dynamic coupling trends between the instantaneous circulation strength Γ' and the temporal modes $a_n(t)$ for $MR = 8164$: (*a*) OSL 1; (*b*) OSL 2; (*c*) OSL 3; (*d*) ISL 1; (*e*) ISL 2; (*f*) ISL 3.

For the ISL,

$$\frac{x}{R_o} \sim 0.75, \quad 0 \leqslant \frac{y}{R_o} \leqslant 1.5, \quad \text{ISL } 1, 2, 3 \rightarrow \text{KH mode.} \tag{5.4a–c}$$

In summary, in this section, we found the mechanism behind the peculiar nature of coherence signatures corresponding to ISL and OSL injections.

6. Breakup dynamics of liquid droplets

In the previous section, we elucidated the dispersion mechanism of the droplets due to flow fluctuations. We will present in this section the droplet breakup processes and regimes as a function of the circulation strengths Γ' and $\overline{\Gamma}$. First, instantaneous

https://doi.org/10.1017/jfm.2017.495 Published online by Cambridge University Press

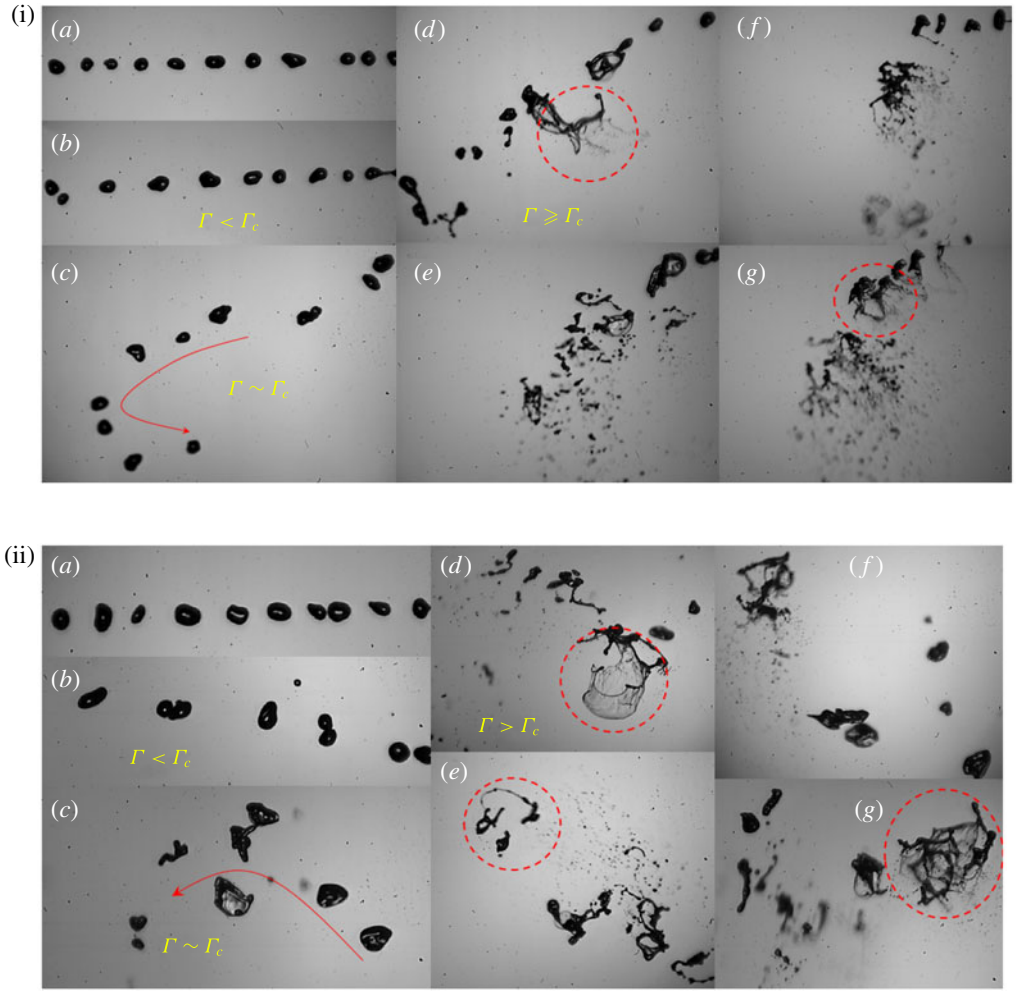

FIGURE 15. (Colour online) Instantaneous visualization of droplet breakup/interaction with vortices: (*a*) $MR \sim 0$; (*b*) $MR \sim 184$; (*c*) $MR \sim 450$; (*d*) $MR \sim 1920$; (*e*) $MR \sim 3720$; (*f*) $MR \sim 5899$; (*g*) $MR \sim 8164$; (i) OSL 2; (ii) ISL 2.

snapshots of the droplet breakup modes are shown, followed by a detailed analysis of the dynamics involved.

6.1. *High-speed visualization of vortex–droplet interaction*

The flow conditions pertaining to two-way, transition and one-way interactions were identified in the global flow field characterization (§ 2). Instantaneous snapshots of droplet images corresponding to these interaction types are shown in figure 15(i),(ii). Interestingly, the interacting droplets exhibit several complicated structures (marked as red circles in figure 15i,ii*d–g*) while breaking up into fragments. The driving mechanism for these breakups includes large-scale coherent structures present in the gas phase and the associated instability modes like KH shear and vortex shedding, as explained in the earlier sections.

https://doi.org/10.1017/jfm.2017.495 Published online by Cambridge University Press

6.2. *Droplet breakup regimes*

The droplets injected into vortices are subjected to oscillations induced by the swirling gas phase flow, leading to shape deformation and breakup. Several experimental and theoretical works (Hanson, Domich & Adams 1963; Simpkins & Bales 1972) have been carried out to elucidate the droplet breakup mechanisms in coflowing air.

In general, the two major forces, namely the aerodynamic drag force (F_a) and the restoring surface tension force (F_σ), involved in the droplet deformation/breakup process can be expressed in non-dimensional form (Weber number We) as follows:

$$We \sim \frac{F_a}{F_\sigma}. \tag{6.1}$$

The aerodynamic force induced by the vortex is given by

$$F_a \sim \rho_a \left(\frac{\overline{\Gamma}}{2\pi \overline{r_{cc}}} \right)^2. \tag{6.2}$$

The detailed derivations and assumptions involved with (6.2) can be found in Oweis *et al.* (2005). Now, expression (6.2) can be rewritten as

$$\overline{We} \sim \frac{\rho_a \left(\dfrac{\overline{\Gamma}}{2\pi \overline{r_{cc}}} \right)^2}{\left(\dfrac{\sigma}{D_o} \right)}. \tag{6.3}$$

Here, $\overline{\Gamma}$ is the time-averaged circulation strength, $\overline{r_{cc}}$ is the vortex core radius obtained from time-averaged flow field images, σ is the interfacial tension and D_o is the initial droplet diameter. In the present experiments, the initial injected droplets are predominantly monodispersed in nature with an average diameter of 500 μm. In addition, an instantaneous Weber number (We') is also proposed as a function of the instantaneous spatially averaged circulation strength (Γ'). Here, We' is evaluated from (6.3) except that Γ' is used instead of $\overline{\Gamma}$.

It should be noted that We' and $\overline{We}$ are calculated in a small spatial window (at the location of first entry of droplets into the flow field, shown in figure S5) rather than around each droplet (which is impossible). The size of the spatial window (which varies with respect to the airflow rate; ∼10 × 10–30 × 30 mm) is chosen in such a way that the values of Γ' and $\overline{\Gamma}$ are largely insensitive to the box size so long it encompasses the high-vorticity region. Therefore, it is assumed that all droplets in that window experience the same circulation at any time instant. Hence, the Weber number is not based on individual droplets but rather on the initial diameter of the droplets entering the spatial window. In summary, $\overline{We}$ is a spatiotemporally averaged parameter, while We' is only a spatially averaged parameter evaluated at any given time instant.

For precise representation, the calculation of We' should involve the instantaneous droplet diameter and the local vortex strength (Γ'). However, this demands simultaneous measurement of individual droplet morphology (shape oscillations), tracking of droplet location and its surrounding flow field. This also requires a sufficiently lower number of droplets (∼1 droplet s^{-1}) in the flow field. All of these are out of the scope of the current work.

In the present study, the droplet breakup can be viewed as two processes, primary and secondary. Primary breakup is the event that occurs where droplets first interact

https://doi.org/10.1017/jfm.2017.495 Published online by Cambridge University Press

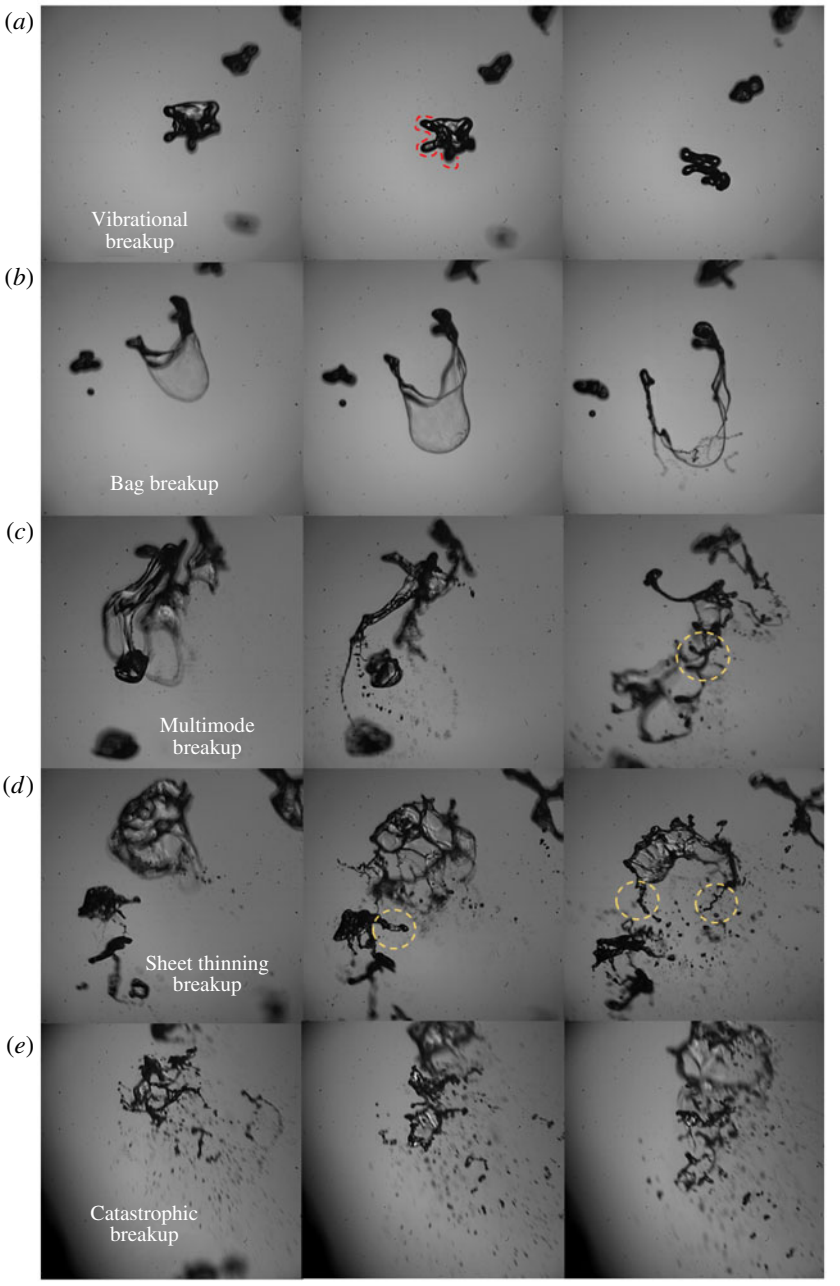

FIGURE 16. (Colour online) Illustration of breakup modes as a function of the time-averaged Weber number: (*a*) ($0 < \overline{We} \leqslant 16$, $0 < MR \leqslant 184$); (*b*) ($16 < \overline{We} \leqslant 57$, $184 < MR \leqslant 450$); (*c*) ($57 < \overline{We} \leqslant 95$, $450 < MR \leqslant 3720$); (*d*) ($95 < \overline{We} \leqslant 335$, $3720 < MR \leqslant 5899$); (*e*) ($335 < \overline{We} \sim 500$, $5899 < MR \leqslant 8164$).

with eddies (mostly large scale) and yield fluid dynamically unstable structures like ligaments, non-spherical droplets, etc. (see the yellow circles in figure 16*c*,*d*).

https://doi.org/10.1017/jfm.2017.495 Published online by Cambridge University Press

These droplets may further undergo breakup (secondary) while interacting with the shedding eddies.

The various breakup modes observed as a function of the Weber number (6.3) are illustrated in figure 16. It should be noted that the breakup modes shown above do not pertain to any particular injection location. They are just sample illustrations of breakup mechanisms common across all injection locations as a function of the Weber number. However, the instantaneous interaction and dispersion mechanisms are found to be tightly coupled functions of the injection location, which will be illustrated in later sections. In common practice, droplet breakup is initiated if the Weber number ($\overline{We}$) exceeds a certain threshold/critical value ($\overline{We}_c$). Theoretically, $\overline{We}_c$ is found to be $\geqslant 10$ (Hinze 1955).

At this value, the waves formed over the droplet surface lead to multimodal shape oscillations (vibrational deformation), which ultimately result in breakup. In situations where lower aerodynamic forcing is involved, $0 < \overline{We} < 16$, the surface tension damps the waves formed over the droplet surface, which mostly results in deformation/pinching of ligaments from the droplet surface (marked as red dotted lines in figure 16*a*). In the current set-up, bag breakup ($16 < \overline{We} < 57$; figure 16*b*) occurs at a transitional Weber number (i.e. low airflow rate). The physical mechanism that governs this process is identified as differential pressure across the front and rear ends of the droplets (Han & Tryggvason 1999).

Multimode breakup (figure 16*c*) is witnessed for $450 < MR \leqslant 1920$. Dai & Faeth (2001) categorized this breakup process as a transition between pressure difference induced bag and shear induced sheet thinning breakup modes. The different forms of breakup modes (vibrational, bag, multimode, sheet thinning, shear/catastrophic breakup) and their physical significance are elaborated in greater detail in Faeth *et al.* (1995) and Guildenbecher *et al.* (2009). The governing mechanism involved with sheet thinning breakup (figure 16*d*) is the formation of a boundary layer over the droplet surface due to the shear induced by fast moving gas (Nicholls & Ranger 1969; Chou, Hsiang & Faeth 1997). It involves deformation of the droplet periphery followed by stretching, formation of ligaments and subsequent breakup into daughter droplets. Catastrophic breakup (figure 16*e*) is mostly encountered in extremely high-shear flows like the current swirling flow field (Hopfinger & Lasheras 1996). In this case, such breakup (figure 16*d*,*e*) is mostly dominated by waves induced by surrounding gas phase instabilities (Taylor 1963; Hsiang & Faeth 1992). The resulting drop sizes in catastrophic breakup predominantly scale with the wavelength λ_{max} that exhibits the highest growth rate.

It is interesting to note that, even for a fixed gas flow rate, different breakup modes are witnessed. For instance, in figure 17(*a*,*b*), it is shown that the flow rate pertaining to $MR \sim 8164$ exhibits several breakup modes like bag, sheet thinning and catastrophic at different time instants. This is due to the fact that fluctuations in the instantaneous circulation (i.e. Γ') eventually lead to large-scale fluctuations in the instantaneous Weber number We'. This phenomenon is graphically illustrated in figure 17(*b*) for $MR \sim 8164$ over one cycle. Here, a cycle is considered based on a time scale ($\tau = 1/f_{KH}$) as calculated from the dominant frequency spectrum obtained from modal analysis (POD).

It can be observed (figure 17*a*) that the instantaneous value of the Weber number shows a large variation (∼10–1050) during any one cycle of vortex shedding even though $\overline{We}$ is much lower (∼400). Hence, it is natural to witness a whole gamut of breakup modes consistent with such Weber number ranges. The average Weber number ($\overline{We}$) would fail to explain the detailed dynamics of droplet breakup in these flows.

https://doi.org/10.1017/jfm.2017.495 Published online by Cambridge University Press

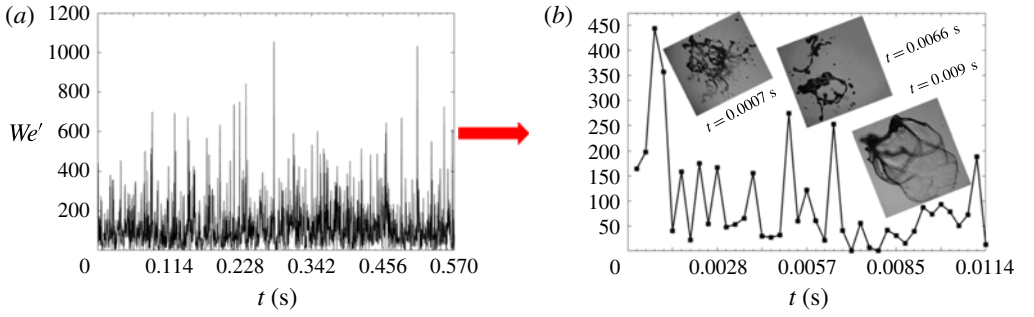

FIGURE 17. (Colour online) (*a*) Illustration of fluctuations observed in We' for a fixed flow rate ($MR \sim 8164$). (*b*) Cyclic behaviour of the Weber number (We') for any given airflow rate ($MR = 8164$).

6.3. *Analysis of droplet eigenmodes*

To evaluate the modal coupling in the droplet breakup process, POD is implemented for instantaneous droplet images acquired from high-speed shadowgraphy. The procedure involved in computing the POD is the same as shown in figure S6. For brevity, only one injection position ($y/R_o = 1$) pertaining to OSL 1 and ISL 1 across three flow conditions (*MR* values) is shown. Similarly to the arguments made in coherence analysis, the eigenmodes (C1–C4) depict dominance of KH shear instability (i.e. mode 1, C1) in both cases. The results at the ISL suggest that even the second mode (C2) is shear dominant (figure 18*b*ii,iii). In contrast, the OSL exhibits shedding and shear as a combined mode. The other two modes (C3 and C4) are identified as helical and shedding modes. All of this modal information quantified from shadow images shows consistent behaviour, as seen in the flow field POD modes (figure 11). In coaxial atomization, it is well known that the atomization is driven by instability waves formed at the liquid–gas interface. The nature of the waves and their length scale (λ_{max}) are solely determined by the source of perturbations (i.e. instabilities) involved in the breakup process. Studies (Liu, Mather & Reitz 1993; Chandrasekhar 2013) have identified that the wave growth over the droplet surface is predominantly described by Rayleigh–Taylor (RT) and KH instabilities.

The KH mode is shown to be a prime cause, where droplets are subjected to large shear like vortices and jets in cross-flow, to name a few (Lasheras, Villermaux & Hopfinger 1998; Marmottant & Villermaux 2004). Subsequently, secondary events like pinching of ligaments, their breakup and formation of daughter droplets are governed by the RT instability. Here, the qualitative information about the dominant wavelength (λ_{max}) can be predicted from POD temporal mode frequency spectra. The most unstable wavelength λ_{max} and frequency f are related as $f_{KH} \approx U_i/\lambda_{max}$, where U_i is the interfacial velocity.

The frequency signatures derived using POD analysis for only the gas phase (A) and for the combined liquid–gas phase (C) are graphically shown in figure 19. Here, the results are presented as a function of the time-averaged Weber number ($\overline{We}$). For low airflow rates ($\overline{We} < \overline{We}_c$), the frequency signature between A and C exhibits a decoupling effect i.e. less dominance of gas phase instabilities (region I). It is to be noted that high frequency values are observed for the liquid phase (~800–1200 Hz); this may be due to the small-scale disturbances imposed due to the dominance of the surface tension σ (Squire 1953; Marmottant & Villermaux 2004). Beyond $\overline{We} \geqslant \overline{We}_c$ (i.e. region III), the dominance of the gas phase results in frequency values closer

https://doi.org/10.1017/jfm.2017.495 Published online by Cambridge University Press

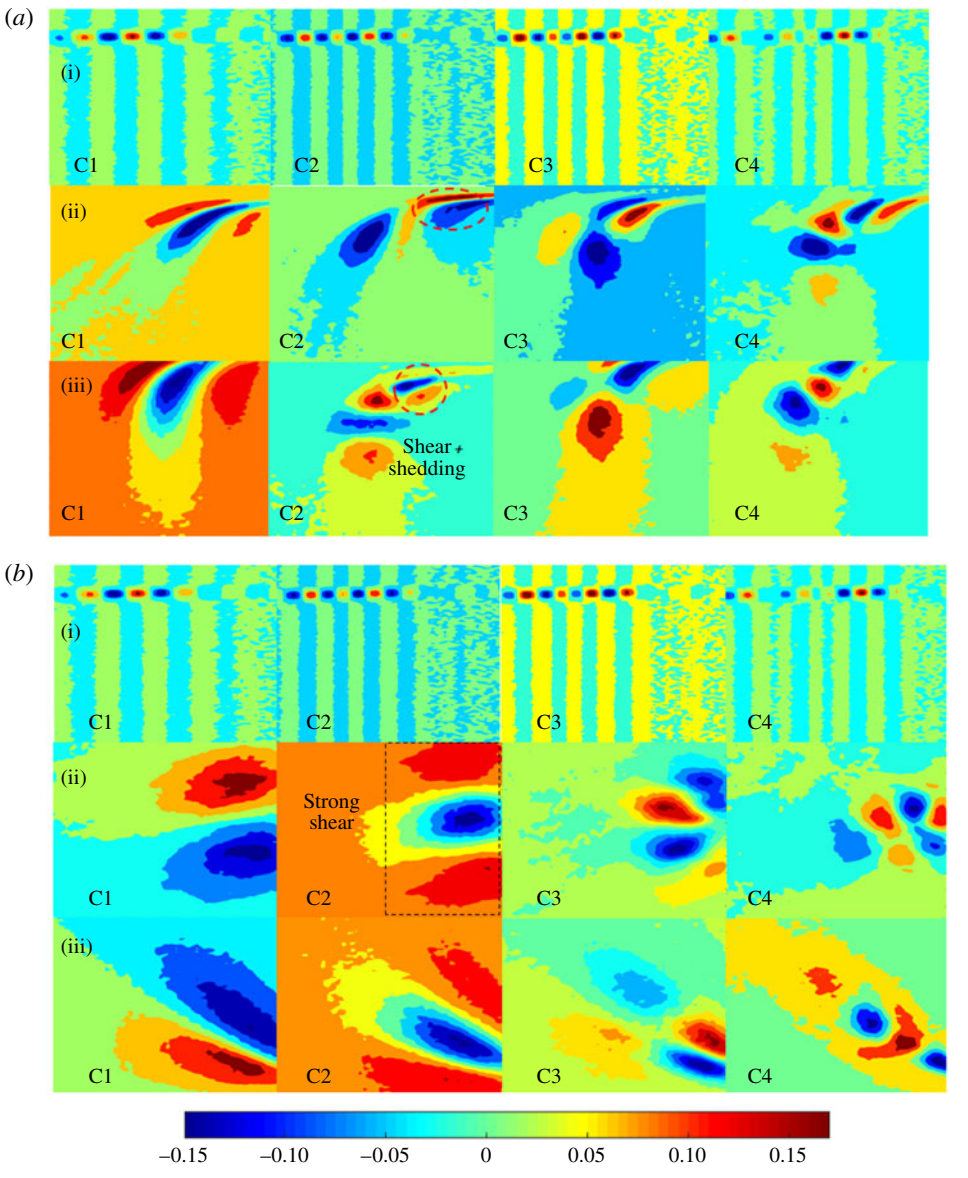

FIGURE 18. (Colour online) Spatial eigenmodes derived from high-speed instantaneous shadow images ($MR = 8164$): (*a*) OSL; (*b*) ISL; (i) OSL 1, ISL 1; (ii) OSL 2, ISL 2; (iii) OSL 3, ISL 3.

to the gas phase instability modes. In particular, the gas phase shear modes are completely synchronized with the droplet breakup process, $f_{A1,A2} \approx f_{C1,C2}$. The lower magnitude of the frequency values observed in regions II and III is due to the long waves (Lasheras & Hopfinger 2000) induced by KH instabilities ($\lambda_{max} \sim \lambda_{KH}$) present in the swirling gas flow field.

In the KH dominated wave region, the speed of propagation of the interface/shear layer (U_i) induced by the most dominant wave can be related to the Dimotakis speed (Cebeci & Bradshaw 1977; Dimotakis 1986).

https://doi.org/10.1017/jfm.2017.495 Published online by Cambridge University Press

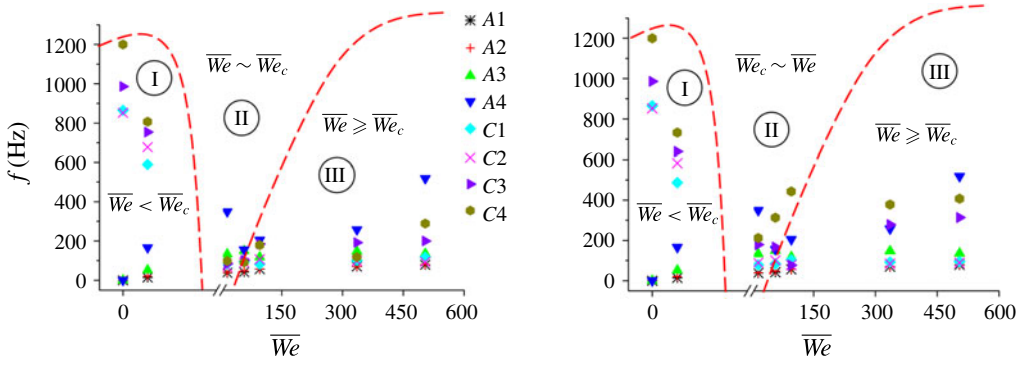

FIGURE 19. (Colour online) Modal frequency signature comparison between the swirling gas phase flow field (*A*) and the high-speed instantaneous shadow images (*C*) of the droplets.

The theoretical expression involves balance of dynamic pressure of the two fluid streams (liquid and gas phases) across the shear layer,

$$\rho_l(V_i - \overline{V_d})_l^2 = \rho_a(\overline{V_\omega} - V_i)_g^2, \tag{6.4}$$

$$V_i \sim \frac{\sqrt{\rho_a}\overline{V_\omega} + \sqrt{\rho_l}\overline{V_d}}{\sqrt{\rho_a} + \sqrt{\rho_l}}, \tag{6.5}$$

where $\overline{V_d}$ and $\overline{V_\omega}$ are the time-averaged velocities of the droplets and vortices; $\overline{V_\omega} = \overline{\Gamma}/2\pi r$. This condition will hold true only when the gas phase is extremely turbulent and the liquid flow is laminar ($\overline{V_\omega} \gg \overline{V_d}$ or $V_i > \overline{V_d}$). The time scale ($\tau = 1/f_{KH}$) pertaining to a cyclic event of the two-phase interaction observed from high-speed shadow images suggests an inline behaviour with Dimotakis speed (6.5). This implies that the acceleration of the interface is predominantly governed by KH waves.

In summary, the primary breakup process is mostly dominated by counter-rotating vortices rather than shedding vortices. However, the shedding vortices may contribute towards further breakup of ligaments/droplets pinched off from the initial droplets during the primary interaction.

The corresponding *MR* values for the aforementioned time-averaged Weber number regimes (I, II, III) are as follows:

(I) $\overline{We} < \overline{We}_c \rightarrow 0 \leqslant MR < 450$, two-way GL–LG regime (movie 6);
(II) $\overline{We} \approx \overline{We}_c \rightarrow 450 < MR \leqslant 1920$, transition to one-way G–L regime (movie 7);
(III) $\overline{We} \geqslant \overline{We}_c \rightarrow 3720 \leqslant MR \leqslant 8164$, strong one-way GL regime (movie 8).

7. Spatial dispersion of droplets in the swirling gas flow field

In liquid-fuelled combustors, important aspects like the mixing field and the dispersed phase homogenization are governed by the interaction dynamics (Moin & Apte 2006; Wang *et al.* 2007). In this section, we begin by presenting results to showcase the mechanism of inhomogeneous dispersion of droplets in the given flow field across the LG–GL and GL interaction conditions. This is more detailed and insightful than the single-parameter dispersion angle analysis (§ 4) from global and local viewpoints. Dispersion of droplets in a given flow field is governed by the

https://doi.org/10.1017/jfm.2017.495 Published online by Cambridge University Press

Stokes number (*St*) (Crowe, Troutt & Chung 1996), which is defined as the ratio between the droplet response time scale (τ_D) and the flow time scale (τ_f),

$$St \sim \frac{\tau_D}{\tau_f}. \tag{7.1}$$

The droplet time scale is a strong function of its diameter (d_o) and can be expressed as

$$\tau_D \sim \frac{\rho_l d^2}{18\mu}. \tag{7.2}$$

The flow time scale can be expressed as a function of the velocity and the characteristic length scale (L) as follows:

$$\tau_f \sim \frac{L}{U}. \tag{7.3}$$

Lazaro & Lasheras (1992) and Longmire & Eaton (1992) have shown that in highly turbulent shear flows, the time scale τ_f is governed by time scales associated with vortical structures induced by instability modes present in the flow field. In particular, the large-scale coherent structures are identified as the prime sources that govern τ_f (Crowe, Chung & Troutt 1988; Hishida, Ando & Maeda 1992). In turbulent shear layers, Aggarwal (1994) has shown that τ_f can be derived from the fundamental frequency of the dominant instability mode. Since, in this study, the KH mode is identified as the dominant instability mechanism, τ_f is defined as

$$\tau_f \sim \frac{1}{f_{KH}}. \tag{7.4}$$

From (7.2)–(7.4), the final expression is written as

$$St \sim \frac{\tau_D}{\tau_f} \sim \left(\frac{\rho_l d^2}{18\mu}\right) * f_{KH}. \tag{7.5}$$

7.1. *Global dispersion field*

The global dispersion field is computed by tracking the individual particles/droplets present in the instantaneous flow field images (acquired with simultaneous PIV). The technique used here computes the spatial location of each droplet present in a given frame (the steps are shown in figure S9). With the computed spatial information (r/R_o', y/R_o) on the droplets, a time-averaged dispersion map (see figure 20*a*,*b* and figure S10*a*,*b*) is generated for the three Weber number regimes (I, II, III) as shown in figure 19. In figure 20, only two representative cases pertaining to OSL and ISL are shown, the remaining cases can be found in the supplementary material (see figure S10).

From figure 20(*a*,*b*), it is perceived that for low Weber numbers, $\overline{We} < \overline{We}_c$, the droplets are not widely dispersed because of low momentum transfer from the gas phase. In this regime (I, II), the breakup process (vibrational, bag) does not yield any smaller sized droplets, which in turn causes the Stokes number to be very high ($St \gg 1$). The quantitative treatment of the Stokes number (*St*) will be elucidated in the size

https://doi.org/10.1017/jfm.2017.495 Published online by Cambridge University Press

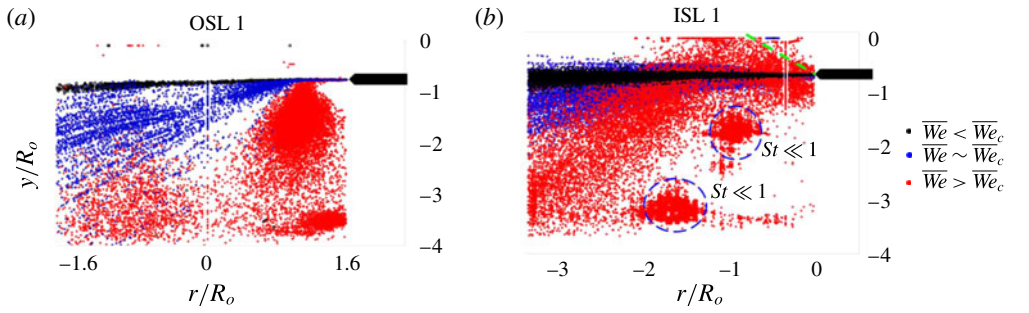

FIGURE 20. (Colour online) The spatial dispersion of the droplets across the three flow regimes (I, II, III): (*a*) OSL 1; (*b*) ISL 1 ($MR = 0$, 450, 8164).

distribution section (see the supplementary material, § 2.5). This ($St \gg 1$) prevents the droplets from dispersing effectively in the flow field. The same mechanism is observed for both OSL and ISL injections. On the contrary, in regime III, the breakup process dominated by gas phase shear instabilities yields several smaller sized droplets (see figure 16*c–e*). Among these smaller sized droplets, those satisfying $St \ll 1$ follow the gas flow path effectively.

(i) Dispersion mechanism in the OSL. In § 5, it is inferred that even for one particular flow rate, fluctuations in Γ' lead to different breakup mechanisms (bag, multimode, catastrophic). In this context, two major forms of dispersion field are observed in the OSL. First, when $\Gamma' < \Gamma'_c$, the injected droplets predominantly do not interact with the vortices and rather penetrate inside the vortex core (figure 21*a*i). In this situation, the droplets are mostly subjected to axial shear, which results in either bag or multimode breakup. This induces very few smaller sized droplets of Stokes number $St < 1$, which are entrained in the recirculation region ($0.5 \leqslant r/R_o \leqslant -0.5$; see figure 21*a*i). On the other hand, when $\Gamma' > \Gamma'_c$, on account of strong interaction with vortices, the droplets undergo catastrophic breakup, which yields a greater number of small-sized droplets. Subsequent to breakup, only the $St \gg 1$ droplets stay in the OSL region ($-0.6 \leqslant r/R_o \leqslant 1.6$; see figure 21*a*ii) due to the resistance offered by high-strength vortices. Moreover, the droplets in these regions tend to disperse radially outwards due to the transfer of gas phase swirl momentum to the droplets. The small-sized droplets ($St < 1$) are entrained in the recirculation region; few droplets of $St \sim 1$ are found to penetrate inside.

(ii) Dispersion mechanism in the ISL. The fundamental difference observed in the dispersion among the ISL and OSL injections is the formation of droplet clusters within the VCC in the ISL region (shown as dotted circles in figures 20*b* and S10*b*). Further, here the droplets are first deflected upwards from the point of injection before they interact with the vortices. In the ISL, as already elucidated in the global flow field section, the vortex strength is not disturbed by injected droplets. This implies that at high airflow rates, the droplets in the ISL are predominantly subjected to shear breakup, which ultimately leads to much smaller droplet sizes. The droplets with Stokes numbers of order $O(\ll 1)$ are trapped inside the recirculation zone (see figure 21*b*). Further downstream of the VCC, the droplets with $St < 1$ are entrained by recirculated flow (indicated as a blue line in figure 21*b*). In addition to the spatial clustering observed with counter-rotating eddies, the shedding eddies contribute to droplet cluster formation (particularly for downstream injections $y/R_o = 1$,

https://doi.org/10.1017/jfm.2017.495 Published online by Cambridge University Press

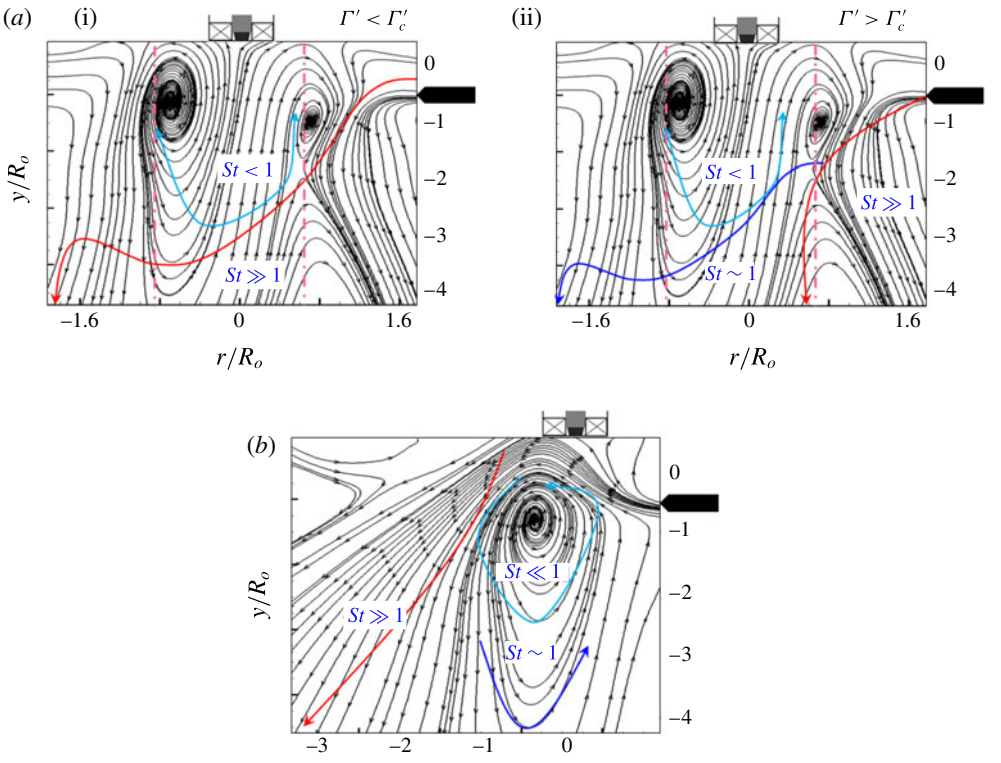

FIGURE 21. (Colour online) The qualitative dispersion mechanisms of the injected droplets in the swirling gas flow field as a function of the Stokes number (St), $MR = 8164$: (*a*) OSL 1; (*b*) ISL 1.

1.5 in figure S10*b*). The remaining droplets ($St \gg 1$) stay in the outside region ($-2 \leqslant r/R_o \leqslant -3$). This clustering of droplets with large-scale eddies creates spatial non-uniformity in the dispersion process. This phenomenon can be viewed as a result of inertial clustering due to the response between the carrier phase and the dispersed phase (Fessler, Kulick & Eaton 1994; Kulick *et al.* 1994).

In addition, the more qualitative nature of the droplet dispersion/response with respect to the swirling gas flow field can be understood from the flow field induced by the droplets. To do this, vector postprocessing is implemented on PIV raw images considering only droplets in the flow field (i.e. without seeding the gas flow). It is well known that in PIV, the flow field can be delineated only if the injected particle response has a linear relationship with the flow time scale (Raffel *et al.* 2013). The vector field reconstructed by considering only droplets in the flow field is shown in the supplementary material (see figure S11) for brevity.

The qualitative view of the spatial dispersion of the droplets in the swirling gas phase flow field is presented in § 7, where the global picture is elucidated as a function of the Stokes number. The more quantitative information in terms of the size distribution is presented in supplementary § 2.5 (figure S12). In figure S12, the droplet size distribution pertaining to region III (i.e. $\overline{We} > \overline{We}_c$) is subdivided into three regimes in terms of the Stokes number (figure S12*b*,*c*). For higher We ($We > 500$), the diameter distribution shows polydisperse characteristics in two predominant ranges of ∼10–20 μm ($St < 1$; see figure S12*b*,*c*) and ∼50–60 μm ($St > 1$) for both ISL and

https://doi.org/10.1017/jfm.2017.495 Published online by Cambridge University Press

OSL injections. The droplet size corresponding to $St < 1$ is identified as the critical diameter ($D_{critical}$). It should be noted that ISL injection exhibits a greater number of $St \ll 1$ droplets than OSL injection (see figure S12*b*,*c*).

8. Spatial homogeneity index

The qualitative treatment of droplet dispersion in the swirling gas flow field is outlined in § 7. Now, we resort to quantitative analysis (i.e. droplet number density in the spatial field), as shown in this section. A parameter called the homogeneity index η is proposed to quantify droplet dispersion in the flow field. Furthermore, the way in which the cyclic fluctuations of We' (circulation strength) result in an instantaneous inhomogeneous dispersion of droplets is elucidated with the phase-averaged dispersion angle.

Garncarek (1993) and Czainski, Garncarek & Piasecki (1994) proposed a statistical tool to identify the homogeneity in the distribution of chosen parameters in a given spatial field. Later, Hayakawa, Okajima & Tokuoka (2008) implemented this approach to evaluate the spatial inhomogeneity in unimodal and bimodal spray interaction processes. Basically, this approach involves discretization of a given spatial field into i windows. Subsequently, one has to define the number of quantities (parameters of interest) present in each window. Mathematically, the inhomogeneity index η is defined as

$$\eta = \sum_{i=1}^{j} \left(n_i - \frac{N}{j} \right)^2, \quad 0 \leqslant \eta \leqslant 1. \tag{8.1}$$

Here, n_i is the number of quantities present in each ith box, N is the sum of all n_i values and j is the total number of boxes. The quantity n_i can be either dimensional or non-dimensional. Here, we treat it as non-dimensional by dividing it by the total sum (i.e. $n_i = N_i/N$). This process is carried out for each instantaneous image (η_i) and summed over all of the images to obtain the time-averaged homogeneity index η.

Essentially, the value of η varies from 0 to 1; the smaller the value is, the higher the dispersion of the droplets is in a given flow field. The spatial flow field is divided into 16 equal-sized windows ($j = 16$) and the number of droplets present in each box is calculated. The 3D spatial inhomogeneity index map is constructed as a function of the Weber number across three axial injection positions (see figure 22). It is seen that η exhibits a monotonic behaviour (decreases linearly) with the Weber number ($\overline{We}$). The obtained results are consistent with the spatial dispersion map shown in figures 20(*a*,*b*) and S10(*a*,*b*).

8.1. *Dispersion-governing parameters*

The instantaneous droplet dispersion and spatial homogeneity may exhibit higher or lower values than the ones shown here in the time-averaged map. The major parameter that governs this process is the local/global Stokes number, which in turn is a function of the fluctuations in the vortex strength induced by gas phase instabilities and the cyclic behaviour of the Weber number in the temporal domain, as already illustrated in figure 17.

In addition, other variables like droplet–droplet and droplet–gas velocity correlations and turbulence modulations are also shown to be parameters responsible for the spatial dispersion (Mashayek 1998; Balachandar & Eaton 2010; Sahu, Hardalupas & Taylor 2014). These effects are not explicitly considered in this study.

https://doi.org/10.1017/jfm.2017.495 Published online by Cambridge University Press

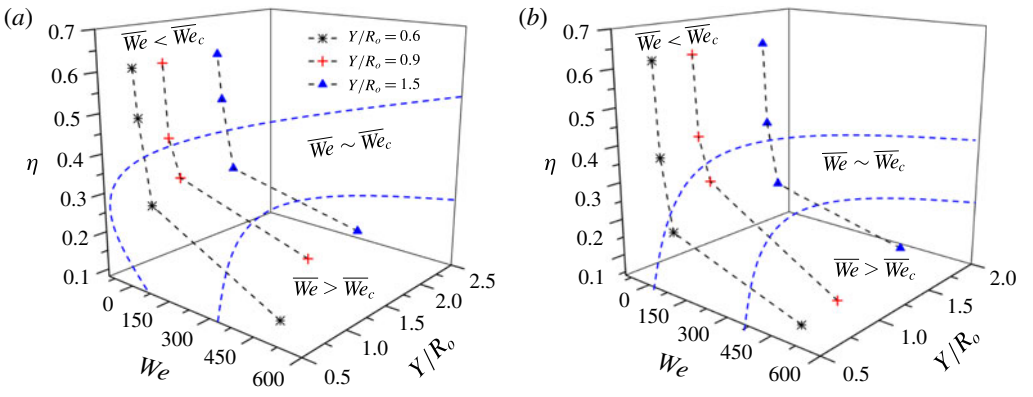

FIGURE 22. (Colour online) Illustration of the spatial inhomogeneity of the droplet dispersion in the swirling gas flow field: (*a*) OSL; (*b*) ISL.

In § 4, it is shown that any perturbation applied to Γ' is reflected in the droplet response θ'. In a given set of time series images, the droplet responses may vary (i.e. phase). For instance, the cyclic behaviour of the Weber number shown in figure 17 exhibits orderly repetitiveness over the time period (see figure 23*a*). To illustrate this phenomenon, the phase-averaged dispersion angle $\overline{\theta}_\emptyset = \sum_{i=1}^{n} (((\theta'_\emptyset)_1 + \cdots + (\theta'_\emptyset)_n)/N)$ is evaluated from the given set of time series images (see figure 23). The dispersion angle corresponding to the peak value observed in each cycle is considered as instantaneous, $\theta'_\emptyset$. The steps involved in the calculation of $\overline{\theta}_\emptyset$ are shown in figure 23(*a*). The graph suggests that the phase-averaged dispersion angle $\overline{\theta}_\emptyset$ differs by a factor of $\sim$10°–15° in GL interaction regimes (III) compared with the time-averaged dispersion angle $\overline{\theta}$. Another influencing parameter is the choice of spatial injection location. Again, both axial and radial positions yield considerable change in the dispersion field. The dispersion of the droplets injected in the near field ($y/R_o \leqslant 1$; OSL 1, 2; ISL 1, 2) is predominantly governed by counter-rotating eddies. On the other hand, the shedding vortices play a significant role in the case of droplets injected at downstream positions ($y/R_o > 1$; OSL 3; ISL 3).

9. Summary and conclusions

The dispersion mechanisms and the breakup of droplets on interaction with large-scale coherent eddies in a swirling gas flow field have been meticulously analysed using time-resolved optical diagnostic tools. In particular, we have reported how the spatial location of the droplet injection influences the flow–droplet coupling and the dispersion mechanism. In this study, droplets were injected as monodispersed streams at certain preselected spatial locations corresponding to the swirl flow field. These positions were chosen near the vortex breakdown bubble and the OSLs, as laid out in figures 2(*a*) and 6. Global flow field characterization (§ 3) was carried out with and without the presence of droplets using time-resolved PIV to establish the momentum coupling process between the gas phase and the droplets. The dynamic pressure (ξ) and the momentum ratio (MR) were used as important global governing parameters to quantify the coupling process. For instance, two-way coupling (LG–GL) was observed for low airflow rates ($0 \leqslant MR < 450$) and transition from two-way LG–GL to one-way GL coupling was observed with progressive increase in the airflow rate ($450 \leqslant MR < 8164$). The airflow rate pertaining to this transition was delineated as the critical

https://doi.org/10.1017/jfm.2017.495 Published online by Cambridge University Press

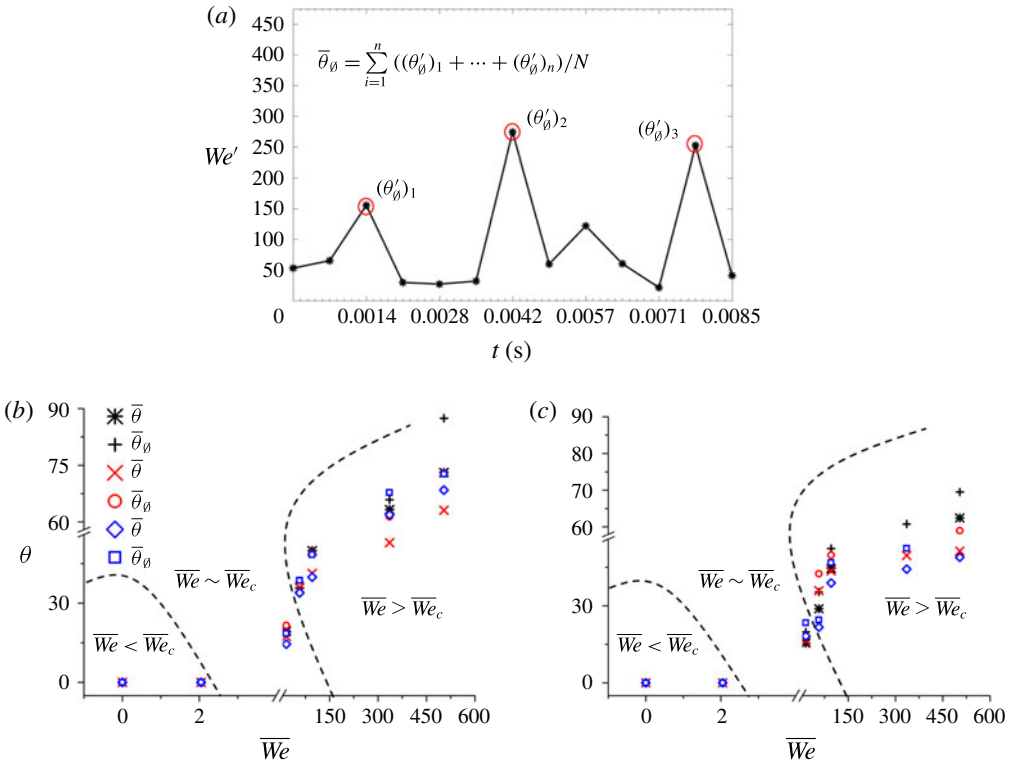

FIGURE 23. (Colour online) (*a*) The steps involved in extraction of the phase-averaged dispersion angle ($\overline{\theta}_{\emptyset}$) are shown over three cycles. (*b*,*c*) Comparison of the time-averaged droplet response ($\overline{\theta}$) with the phase-averaged ($\overline{\theta}_{\emptyset}$) response for (*b*) OSL 2 and (*c*) ISL 2.

momentum ratio MR_c. The abovementioned observations are pictorially illustrated in figure 24. In addition, the local disruption of the vortex core with respect to the injection location is also delineated using the time-averaged flow field.

Subsequently, coherence analysis was carried out to reveal the dynamic correlation between the circulation strength (Γ') of the vortices and the droplet dispersion angle θ'. The results revealed that the droplets injected at both the OSL and the ISL predominantly exhibited high coherence values $\{C_{\Gamma'\theta'}(f) \sim 0.9\}$ around ∼80–100 Hz. However, in addition, droplets at OSL 2, 3 showed intermediate coherence values (∼0.5) at 400–700 Hz. To understand this behaviour, POD was implemented over the instantaneous flow field to extract the contribution of the principal energetic coherent structures of the gas flow. The TKE spectra (eigenmodes) from the POD exhibited dominance of the KH mode (∼80 % of total energy) in ISL 1–3 and OSL 1, and combined action of the KH mode and the shedding mode was observed in OSL 2, 3 (see figure 24). In addition, the coherence analysis carried out between the POD temporal modes and θ' revealed the physical mechanism of modal coupling between the flow circulation and the dispersion at multiple frequencies.

Next, the droplet breakup dynamics was visualized using a high-speed shadow imaging technique. The results were presented as a function of the Weber number defined based on instantaneous and time-averaged circulation strengths, Γ' and $\overline{\Gamma}$. No significant breakup was observed in the LG–GL coupling regime; rather, droplets were subjected to shape oscillation/deformation. For critical airflow rates

https://doi.org/10.1017/jfm.2017.495 Published online by Cambridge University Press

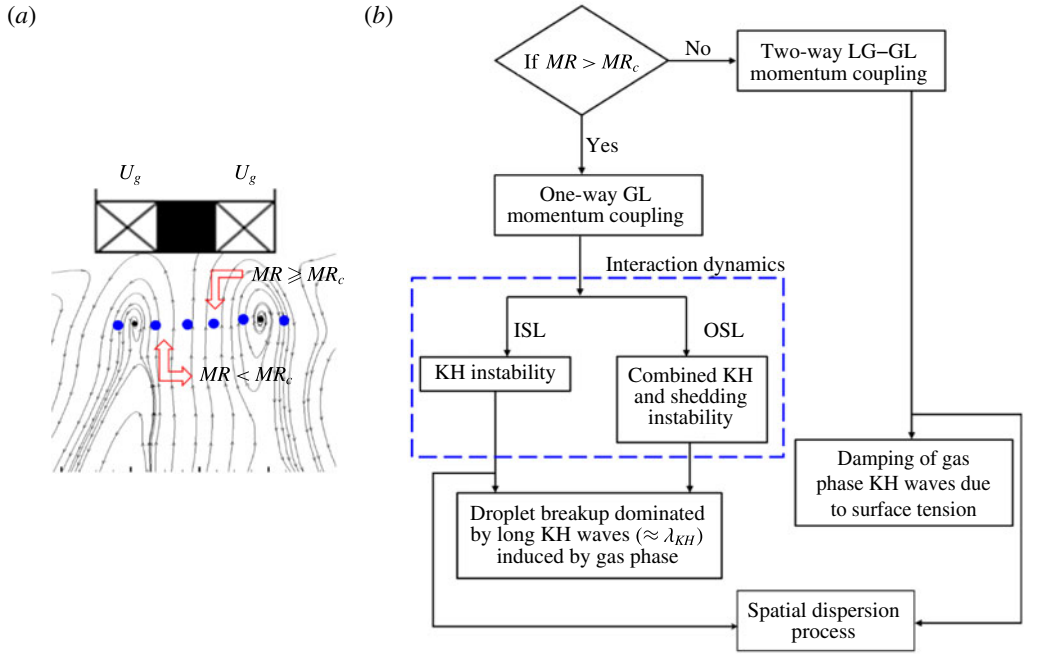

FIGURE 24. (Colour online) Illustration of the key processes involved in droplet–vortex interaction in a swirling gas flow field.

(MR_c; $16 < \overline{We} \leqslant 57$), the bag breakup process was witnessed. The Weber number corresponding to this condition is delineated as $\overline{We}_c$. Beyond $\overline{We}_c$, the droplets predominantly showed sheet thinning ($95 < \overline{We} \leqslant 335$) and catastrophic breakup ($335 < \overline{We} \leqslant 500$) processes. For the first time, it has been showcased that the temporal oscillations of the Weber number We' lead to different breakup mechanisms even for fixed airflow rates (fixed MR).

Finally, the global dispersion map and the mechanisms of dispersion across the ISL and the OSL were delineated as a function of the Stokes number (St). During GL coupling, the droplet dispersion retraces the swirling gas flow path. This is due to the attenuation of long KH waves in the breakup dynamics. For low MR values, the droplet response time scales are not correlated with the flow time scale during LG–GL conditions. In particular, two different key observations were made in the OSL and the ISL.

(i) In ISL injection, the droplets undergo breakup before they reaches the rotating eddies. This pre-breakup of droplets induces a drastic reduction in size, which ultimately leads to lower local Stokes number. Due to this event, the extremely small-sized droplets are trapped in the vortex core (figures S8*b* and 20*b*).

(ii) The same is not observed with OSL injection, where the droplets are deflected away from the vortices.

Acknowledgements

Financial support from the DST under the Swarnajayanti Fellowship (DST/SJF/ETA-02/2013-14) scheme and the National Centre for Combustion Research and Development (NCCRD) is gratefully acknowledged.

https://doi.org/10.1017/jfm.2017.495 Published online by Cambridge University Press

Supplementary movies

Supplementary movies are available at https://doi.org/10.1017/jfm.2017.495.

REFERENCES

ADRIAN, R. J. 1991 Particle-imaging techniques for experimental fluid mechanics. *Annu. Rev. Fluid Mech.* **23**, 261–304.

AGGARWAL, S. K. 1994 Relationship between Stokes number and intrinsic frequencies in particle-laden flows. *AIAA J.* **32**, 1322–1325.

AGGARWAL, S. K. & PARK, T. W. 1999 Dispersion of evaporating droplets in a swirling axisymmetric jet. *AIAA J.* **37**, 1578–1587.

AL TAWEEL, A. M. & LANDAU, J. 1977 Turbulence modulation in two-phase jets. *Intl J. Multiphase Flow* **3**, 341–351.

ALBRECHT, H.-E., DAMASCHKE, N., BORYS, M. & TROPEA, C. 2013 *Laser Doppler and Phase Doppler Measurement Techniques*. Springer.

BALACHANDAR, S. & EATON, J. K. 2010 Turbulent dispersed multiphase flow. *Annu. Rev. Fluid Mech.* **42**, 111–133.

BEÉR, J. M. & CHIGIER, N. A. 1972 *Combustion Aerodynamics*. Applied Science Publishers Ltd.

BENDAT, J. S. & PIERSOL, A. G. 1980 *Engineering Applications of Correlation and Spectral Analysis*. Wiley-Interscience.

BENJAMIN, T. B. 1962 Theory of the vortex breakdown phenomenon. *J. Fluid Mech.* **14**, 593–629.

BERKOOZ, G., HOLMES, P. & LUMLEY, J. L. 1993 The proper orthogonal decomposition in the analysis of turbulent flows. *Annu. Rev. Fluid Mech.* **25**, 539–575.

BILLANT, P., CHOMAZ, J.-M. & HUERRE, P. 1998 Experimental study of vortex breakdown in swirling jets. *J. Fluid Mech.* **376**, 183–219.

BOILEAU, M., PASCAUD, S., RIBER, E., CUENOT, B., GICQUEL, L. Y. M., POINSOT, T. J. & CAZALENS, M. 2008 Investigation of two-fluid methods for large eddy simulation of spray combustion in gas turbines. *Flow Turbul. Combust.* **80**, 291–321.

CEBECI, T. & BRADSHAW, P. 1977 *Momentum Transfer in Boundary Layers*. McGraw-Hill.

CHAMPAGNE, F. H. & KROMAT, S. 2000 Experiments on the formation of a recirculation zone in swirling coaxial jets. *Exp. Fluids* **29**, 494–504.

CHANDRASEKHAR, S. 2013 *Hydrodynamic and Hydromagnetic Stability*. Courier Corporation.

CHIGIER, N. A. & CHERVINSKY, A. 1967 Experimental investigation of swirling vortex motion in jets. *Trans. ASME J. Appl. Mech.* **34**, 443–451.

CHOU, W.-H., HSIANG, L.-P. & FAETH, G. M. 1997 Temporal properties of drop breakup in the shear breakup regime. *Intl J. Multiphase Flow* **23**, 651–669.

CHUNG, J. N. & TROUTT, T. R. 1988 Simulation of particle dispersion in an axisymmetric jet. *J. Fluid Mech.* **186**, 199–222.

COLES, D. 1965 Transition in circular Couette flow. *J. Fluid Mech.* **21**, 385–425.

CROWE, C. T., CHUNG, J. N. & TROUTT, T. R. 1988 Particle mixing in free shear flows. *Prog. Energy Combust. Sci.* **14**, 171–194.

CROWE, C. T., SOMMERFELD, M. & TSUJI, Y. 1998 *Fundamentals of Gas–Particle and Gas–Droplet Flows*. CRC.

CROWE, C. T., TROUTT, T. R. & CHUNG, J. N. 1996 Numerical models for two-phase turbulent flows. *Annu. Rev. Fluid Mech.* **28**, 11–43.

CZAINSKI, A., GARNCAREK, Z. & PIASECKI, R. 1994 Quantitative characterization of inhomogeneity in thin metallic films using Garncarek's method. *J. Phys. D: Appl. Phys.* **27** (3), 616–622.

DAI, Z. & FAETH, G. M. 2001 Temporal properties of secondary drop breakup in the multimode breakup regime. *Intl J. Multiphase Flow* **27**, 217–236.

DANON, H., WOLFSHTEIN, M. & HETSRONI, G. 1977 Numerical calculations of two-phase turbulent round jet. *Intl J. Multiphase Flow* **3**, 223–234.

DIMOTAKIS, P. E. 1986 Two-dimensional shear-layer entrainment. *AIAA J.* **24**, 1791–1796.

https://doi.org/10.1017/jfm.2017.495 Published online by Cambridge University Press

ELGHOBASHI, S. E. & ABOU-ARAB, T. W. 1983 A two-equation turbulence model for two-phase flows. *Phys. Fluids* **26**, 931–938.

ELGHOBASHI, S. & TRUESDELL, G. C. 1993 On the two-way interaction between homogeneous turbulence and dispersed solid particles. I: turbulence modification. *Phys. Fluids Fluid Dyn.* **5**, 1790–1801.

ENGELBERT, C., HARDALUPAS, Y. & WHITELAW, J. H. 1995 Breakup phenomena in coaxial airblast atomizers. In *Proceedings of the Royal Society of London A: Mathematical, Physical and Engineering Sciences*, pp. 189–229. The Royal Society.

FAETH, G. M., HSIANG, L.-P. & WU, P.-K. 1995 Structure and breakup properties of sprays. *Intl J. Multiphase Flow* **21**, 99–127.

FESSLER, J. R., KULICK, J. D. & EATON, J. K. 1994 Preferential concentration of heavy particles in a turbulent channel flow. *Phys. Fluids* **6**, 3742–3749.

FLOCK, A. K., GUILDENBECHER, D. R., CHEN, J., SOJKA, P. E. & BAUER, H.-J. 2012 Experimental statistics of droplet trajectory and air flow during aerodynamic fragmentation of liquid drops. *Intl J. Multiphase Flow* **47**, 37–49.

GALLAIRE, F. & CHOMAZ, J.-M. 2003 Instability mechanisms in swirling flows. *Phys. Fluids* **15**, 2622–2639.

GARNCAREK, Z. 1993 Constructions of the measures of distribution features for finite point sets with examples of applications in natural and technical sciences. ZN WSP Opole Stud. Monogr. NR 203, 1–114.

GILLANDT, I., FRITSCHING, U. & BAUCKHAGE, K. 2001 Measurement of phase interaction in dispersed gas/particle two-phase flow. *Intl J. Multiphase Flow* **27**, 1313–1332.

GU, X., BASU, S. & KUMAR, R. 2012 Dispersion and vaporization of biofuels and conventional fuels in a crossflow pre-mixer. *Intl J. Heat Mass Transfer* **55**, 336–346.

GUILDENBECHER, D. R., LÓPEZ-RIVERA, C. & SOJKA, P. E. 2009 Secondary atomization. *Exp. Fluids* **46**, 371–402.

HALL, M. G. 1967 A new approach to vortex breakdown. In *14th Atmospheric Flight Mechanics Conference*, pp. 319–340. *AIAA Paper* 1987-2495.

HAN, J. & TRYGGVASON, G. 1999 Secondary breakup of axisymmetric liquid drops. I. Acceleration by a constant body force. *Phys. Fluids* **11**, 3650–3667.

HANSON, A. R., DOMICH, E. G. & ADAMS, H. S. 1963 Shock tube investigation of the breakup of drops by air blasts. *Phys. Fluids* **6**, 1070–1080.

HAYAKAWA, S., OKAJIMA, S. & TOKUOKA, N. 2008 The study of spray structure by numerical simulation – the effect of interaction between droplets on spatial inhomogeneity. In *22nd European Conference on Liquid Atomization and Spray Systems 8–10 September 2008, Como Lake, Italy*, ILASS-Europe.

HINZE, J. O. 1955 Fundamentals of the hydrodynamic mechanism of splitting in dispersion processes. *AIChE J.* **1**, 289–295.

HISHIDA, K., ANDO, A. & MAEDA, M. 1992 Experiments on particle dispersion in a turbulent mixing layer. *Intl J. Multiphase Flow* **18**, 181–194.

HOPFINGER, E. J. & LASHERAS, J. C. 1996 Explosive breakup of a liquid jet by a swirling coaxial gas jet. *Phys. Fluids* **8**, 1696–1698.

HSIANG, L.-P. & FAETH, G. M. 1992 Near-limit drop deformation and secondary breakup. *Intl J. Multiphase Flow* **18**, 635–652.

KEANE, R. D. & ADRIAN, R. J. 1990 Optimization of particle image velocimeters. I. Double pulsed systems. *Meas. Sci. Technol.* **1**, 1202.

KHALITOV, D. A. & LONGMIRE, E. K. 2002 Simultaneous two-phase PIV by two-parameter phase discrimination. *Exp. Fluids* **32**, 252–268.

KHALITOV, D. A. & LONGMIRE, E. K. 2003 Effect of particle size on velocity correlations in turbulent channel flow. In *ASME/JSME 2003 4th Joint Fluids Summer Engineering Conference*, pp. 445–453. American Society of Mechanical Engineers.

KOSIWCZUK, W., CESSOU, A., TRINITE, M. & LECORDIER, B. 2005 Simultaneous velocity field measurements in two-phase flows for turbulent mixing of sprays by means of two-phase PIV. *Exp. Fluids* **39**, 895–908.

https://doi.org/10.1017/jfm.2017.495 Published online by Cambridge University Press

KULICK, J. D., FESSLER, J. R. & EATON, J. K. 1994 Particle response and turbulence modification in fully developed channel flow. *J. Fluid Mech.* **277**, 109–134.

LASHERAS, J. C. & HOPFINGER, E. J. 2000 Liquid jet instability and atomization in a coaxial gas stream. *Annu. Rev. Fluid Mech.* **32**, 275–308.

LASHERAS, J. C., VILLERMAUX, E. & HOPFINGER, E. J. 1998 Break-up and atomization of a round water jet by a high-speed annular air jet. *J. Fluid Mech.* **357**, 351–379.

LAZARO, B. J. & LASHERAS, J. C. 1992 Particle dispersion in the developing free shear layer. Part 1. Unforced flow. *J. Fluid Mech.* **235**, 143–178.

LEFEBVRE, A. H. 2010 *Gas Turbine Combustion*. CRC.

LIANG, H. & MAXWORTHY, T. 2005 An experimental investigation of swirling jets. *J. Fluid Mech.* **525**, 115–159.

LILLEY, D. G. 1977 Swirl flows in combustion: a review. *AIAA J.* **15**, 1063–1078.

LIU, A. B., MATHER, D. & REITZ, R. D. 1993 Modeling the effects of drop drag and breakup on fuel sprays. DTIC Document.

LONGMIRE, E. K. & EATON, J. K. 1992 Structure of a particle-laden round jet. *J. Fluid Mech.* **236**, 217–257.

LOTH, E., TRYGGVASON, G., TSUJI, Y., ELGHOBASHI, S. E., CROWE, C. T., BERLEMONT, A., REEKS, M., SIMONIN, O., FRANK, T., ONISHI, Y. *et al.* 2006 *Multiphase Flow Handbook*. CRC.

LOZANO, A., BARRERAS, F., SIEGLER, C. & LÖW, D. 2005 The effects of sheet thickness on the oscillation of an air-blasted liquid sheet. *Exp. Fluids* **39**, 127–139.

LUCCA-NEGRO, O. & O'DOHERTY, T. 2001 Vortex breakdown: a review. *Prog. Energy Combust. Sci.* **27**, 431–481.

MARMOTTANT, P. & VILLERMAUX, E. 2004 On spray formation. *J. Fluid Mech.* **498**, 73–111.

MARTINELLI, F., OLIVANI, A. & COGHE, A. 2007 Experimental analysis of the precessing vortex core in a free swirling jet. *Exp. Fluids* **42**, 827–839.

MASHAYEK, F. 1998 Droplet–turbulence interactions in low-Mach-number homogeneous shear two-phase flows. *J. Fluid Mech.* **367**, 163–203.

MOIN, P. & APTE, S. V. 2006 Large-eddy simulation of realistic gas turbine combustors. *AIAA J.* **44**, 698–708.

NICHOLLS, J. A. & RANGER, A. A. 1969 Aerodynamic shattering of liquid drops. *AIAA J.* **7**, 285–290.

OWEIS, G. F., VAN DER HOUT, I. E., IYER, C., TRYGGVASON, G. & CECCIO, S. L. 2005 Capture and inception of bubbles near line vortices. *Phys. Fluids* **17**, 022105.

PARK, T. W., KATTA, V. R. & AGGARWAL, S. K. 1998 On the dynamics of a two-phase, nonevaporating swirling jet. *Intl J. Multiphase Flow* **24**, 295–317.

RAFFEL, M., WILLERT, C. E., WERELEY, S. & KOMPENHANS, J. 2013 *Particle Image Velocimetry: A Practical Guide*. Springer.

RAJAMANICKAM, K. & BASU, S. 2017 Insights into the dynamics of spray–swirl interactions. *J. Fluid Mech.* **810**, 82–126.

RIBEIRO, M. M. & WHITELAW, J. H. 1980 Coaxial jets with and without swirl. *J. Fluid Mech.* **96**, 769–795.

SAHA, A., LEE, J. D., BASU, S. & KUMAR, R. 2012 Breakup and coalescence characteristics of a hollow cone swirling spray. *Phys. Fluids* **24**, 124103.

SAHU, S., HARDALUPAS, Y. & TAYLOR, A. 2014 Droplet–turbulence interaction in a confined polydispersed spray: effect of droplet size and flow length scales on spatial droplet–gas velocity correlations. *J. Fluid Mech.* **741**, 98–138.

SAKAKIBARA, J., WICKER, R. B. & EATON, J. K. 1996 Measurements of the particle–fluid velocity correlation and the extra dissipation in a round jet. *Intl J. Multiphase Flow* **22**, 863–881.

SANADI, D., RAJAMANICKAM, K. & BASU, S. 2017 Analysis of hollow cone spray injected in an unconfined, isothermal, co-annular swirling jet environment. *Atomization and Sprays* **27**, 7–29.

SANKARAN, V. & MENON, S. 2002 LES of spray combustion in swirling flows. *J. Turbul.* **3**, 1–23.

SANTHOSH, R., MIGLANI, A. & BASU, S. 2014 Transition in vortex breakdown modes in a coaxial isothermal unconfined swirling jet. *Phys. Fluids* **26**, 043601.

https://doi.org/10.1017/jfm.2017.495 Published online by Cambridge University Press

SARPKAYA, T. 1971 On stationary and travelling vortex breakdowns. *J. Fluid Mech.* **45**, 545–559.

SCHRÖDER, A., GEISLER, R., STAACK, K., ELSINGA, G. E., SCARANO, F., WIENEKE, B., HENNING, A., POELMA, C. & WESTERWEEL, J. 2011 Eulerian and Lagrangian views of a turbulent boundary layer flow using time-resolved tomographic PIV. *Exp. Fluids* **50**, 1071–1091.

SCIACCHITANO, A., WIENEKE, B. & SCARANO, F. 2013 PIV uncertainty quantification by image matching. *Meas. Sci. Technol.* **24**, 045302.

SHIROLKAR, J. S., COIMBRA, C. F. M. & MCQUAY, M. Q. 1996 Fundamental aspects of modeling turbulent particle dispersion in dilute flows. *Prog. Energy Combust. Sci.* **22**, 363–399.

SIMPKINS, P. G. & BALES, E. L. 1972 Water-drop response to sudden accelerations. *J. Fluid Mech.* **55**, 629–639.

SIRIGNANO, W. A. 1999 *Fluid Dynamics and Transport of Droplets and Sprays*. Cambridge University Press.

SIROVICH, L. 1987 Turbulence and the dynamics of coherent structures. Part I: coherent structures. *Q. Appl. Maths* **45**, 561–571.

SQUIRE, H. B. 1953 Investigation of the instability of a moving liquid film. *Brit. J. Appl. Phys.* **4**, 167.

SUNG, J. & YOO, J. Y. 2001 Three-dimensional phase averaging of time-resolved PIV measurement data. *Meas. Sci. Technol.* **12**, 655.

SYRED, N. 2006 A review of oscillation mechanisms and the role of the precessing vortex core (PVC) in swirl combustion systems. *Prog. Energy Combust. Sci.* **32**, 93–161.

TAYLOR, G. I. 1963 The shape and acceleration of a drop in a high speed air stream. In *Scientific Papers of G. I. Taylor* (ed. G. K. Batchelor), vol. 3, pp. 457–464. Cambridge University Press.

TROPEA, C., YARIN, A. L. & FOSS, J. F. 2007 *Springer Handbook of Experimental Fluid Mechanics*. Springer.

WANG, H. Y., MCDONELL, V. G. & SAMUELSEN, S. 1993 Influence of hardware design on the flow field structures and the patterns of droplet dispersion: Part I – mean quantities. In *ASME 1993 International Gas Turbine and Aeroengine Congress and Exposition*, p. V03AT15A050. American Society of Mechanical Engineers.

WANG, S., YANG, V., HSIAO, G., HSIEH, S.-Y. & MONGIA, H. C. 2007 Large-eddy simulations of gas-turbine swirl injector flow dynamics. *J. Fluid Mech.* **583**, 1–10.

WIENEKE, B. 2015 PIV uncertainty quantification from correlation statistics. *Meas. Sci. Technol.* **26**, 074002.

https://doi.org/10.1017/jfm.2017.495 Published online by Cambridge University Press